JACS
JOURNAL OF THE AMERICAN CHEMICAL SOCIETY

ARTICLE

pubs.acs.org/JACS

Hyperbranched Anatase TiO_2 Nanocrystals: Nonaqueous Synthesis, Growth Mechanism, and Exploitation in Dye-Sensitized Solar Cells

Raffaella Buonsanti,[†,#] Elvio Carlino,[‡] Cinzia Giannini,[§] Davide Altamura,[§] Luisa De Marco,[∥]
Roberto Giannuzzi,[∥] Michele Manca,[∥] Giuseppe Gigli,[†,⊥] and P. Davide Cozzoli*[,†,⊥]

[†]National Nanotechnology Laboratory (NNL), Istituto Nanoscienze CNR, c/o Distretto Tecnologico, via per Arnesano km 5, 73100 Lecce, Italy

[‡]TASC National Laboratory, IOM-CNR, Area Science Park - Basovizza, Building MM, SS 14, Km 163.5, 34149 Trieste, Italy

[§]Istituto di Crystallografia (IC−CNR), via Amendola 122/O, I-70126 bari, Italy

[∥]Center for Biomolecular Nanotechnologies - Italian Institute of Technology (IIT), c/o Stamms, via Barsanti, 73010 Arnesano (Lecce), Italy

[⊥]Dipartimento di Ingegneria dell'Innovazione, Università del Salento, via per Arnesano, 73100 Lecce, Italy

Supporting Information

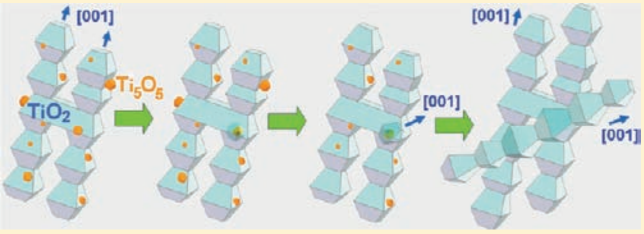

ABSTRACT: A colloidal crystal-splitting growth regime has been accessed, in which TiO_2 nanocrystals, selectively trapped in the metastable anatase phase, can evolve to anisotropic shapes with tunable hyperbranched topologies over a broad size interval. The synthetic strategy relies on a nonaqueous sol−gel route involving programmed activation of aminolysis and pyrolysis of titanium carboxylate complexes in hot surfactant media via a simple multi-injection reactant delivery technique. Detailed investigations indicate that the branched objects initially formed upon the aminolysis reaction possess a strained monocrystalline skeleton, while their corresponding larger derivatives grown in the subsequent pyrolysis stage accommodate additional arms crystallographically decoupled from the lattice underneath. The complex evolution of the nanoarchitectures is rationalized within the frame of complementary mechanistic arguments. Thermodynamic pathways, determined by the shape-directing effect of the anatase structure and free-energy changes accompanying branching and anisotropic development, are considered to interplay with kinetic processes, related to diffusion-limited, spatially inhomogeneous monomer fluxes, lattice symmetry breaking at transient Ti_5O_5 domains, and surfactant-induced stabilization. Finally, as a proof of functionality, the fabrication of dye-sensitized solar cells based on thin-film photoelectrodes that incorporate networked branched nanocrystals with intact crystal structure and geometric features is demonstrated. An energy conversion efficiency of 6.2% has been achieved with standard device configuration, which significantly overcomes the best performance ever approached with previously documented prototypes of split TiO_2 nanostructures. Analysis of the relevant photovoltaic parameters reveals that the utilized branched building blocks indeed offer light-harvesting and charge-collecting properties that can overwhelm detrimental electron losses due to recombination and trapping events.

1. INTRODUCTION

The development of flexibly processable inorganic nanostructures with programmable structural−compositional parameters and surface functionalities represents an essential transition pathway toward realization of the technological prospects offered by their unique chemical-physical behavior.[1] As of today, colloidal routes have enabled access to an exceptionally broad variety of single- to multicomponent nanocrystals with controlled isotropic (spheres, cubes, polyhedrons), linear (rods, wires, tubes, rings), or planar (platelets, sheets) morphologies, which exhibit tailored properties and predictable performances in processes and devices.[2−5] Recent synthetic advances have further enriched the colloidal realm with spatially elaborate breeds of branched nanocrystals (BNCs), which embody one-dimensional arm sections interconnected through branch junctions into complex split architectures.[2,3,5,6] BNCs have indeed been recognized to offer distinguished chemical,[7−10] mechanical,[11] optical,[5,11,12] and magnetic properties,[13,14] which have been purposely exploited in applications as diverse as catalysis,[7,8,15,16] photovoltaics,[5,11,17−19] nanoelectronics,[11] scanning probe microscopy,[11] and biomedical imaging.[20]

In colloidal media, branching can originate from disparate symmetry-breaking mechanisms that may intervene in distinct stages of nanocrystal evolution.[2−4,6] Operation of these pathways, most of which are yet far from being fully understood or

Received: September 9, 2011
Published: October 17, 2011

even experimentally identifiable, depends on the crystal structure of the concerned material and on the particular kinetic regime dictated by the synthesis conditions. For example, BNCs of cubic-phase compounds (e.g., metal chalcogenides, transition metals, and oxides) have frequently been shaped into urchin-, star-, and dendrite-like habits by exploiting ligand-assisted facet-competitive development,[2,4,6,11,12,13a,13c,15,21] oriented attachment,[2,4,6,13b,21] or directional etching of primary isotropic particles.[4b,6,12,14] Shaping resulting from growth deviations triggered by lattice defects[2−4,6,16] or foreign catalyst seeds[6,21,22] has also been assessed. Polytypic BNCs in the form of polypods that incorporate stacked domains of different phases at the branch points and arm sections, respectively, have been achieved in the case of materials (e.g., metal chalcogenides) for which the relative stability of the possible polymorphs reverses during their formation.[2,4a,11] In other, less common circumstances, BNCs entirely trapped in asymmetric crystal structures (e.g., metal chalcogenides, phosphides, sulfates, and oxides) have been found to adopt open ramified skeletons assembled around multiply twinned embryos[2,4,11,23,24] or take dense-packed filamentous bundle-, sheaf-, or spherulite-like morphologies through a mechanism of abrupt lattice splitting, analogous to that occurring in natural mineralization.[25] Multicomponent heterostructured BNCs have also been produced by seed-mediated approaches, in which preformed nanocrystals act as initial substrates from which branch sections with dissimilar composition and/or crystal structure depart out upon heterogeneous nucleation.[2,5,11,21]

To date, although a large library of ramified nanocrystal architectures has become available, the chemical synthesis and practical exploitation of BNCs made of transition-metal oxides have attained limited success. Progress in this field promises not only to consolidate the fundamental comprehension of the mechanisms underlying nanocrystal branching, but also to open up new technological opportunities based on the exploitation of the extraordinary solid-state properties that characterize these materials on the nanoscale.[3] Among oxides, semiconductor TiO_2 notoriously holds unparallel potential in a variety of cost-effective and environmentally friendly solutions to renewable energy resources and processes.[26] In particular, colloidal TiO_2 nano structures are being sought after as flexibly utilizable building blocks for the fabrication of mesoporous thin-film photoelectrodes that are at the heart of third-generation photovoltaic devices, such as dye-sensitized solar cells (DSSCs).[26,27] The ability to create photoanodes in which the structural and morphological features of the underlying TiO_2 nanocrystal constituents provide tailored nanotexture with a higher degree of functionality represents an indispensible step toward boosting the ultimate light-to-electricity conversion.[28]

Novel breeds of TiO_2 BNCs with unconventional architectures that integrate linear segments through branch-type connectivity are now being sought after as effective key elements for realizing advanced DSSCs that can potentially profit from superior electron transport and interfacial charge-transfer properties, as compared to those achievable with their isotropic nanocrystal counterparts.[28] Specific advantages promised by photoelectrodes that embody anisotropically shaped TiO_2 building blocks with split topologies, in which single-domain arm sections are already interlaced prior to the sintering step via bonding interfaces, include, on one side, enhanced electron diffusion facilitated by the availability of extended percolation pathways along preferential lattice directions and, on the other side, decreased density of charge-trapping states associated with crystal defects in the lattice or, more frequently, at contact grain boundaries across the oxide network.[17−19,29,30] All these benefits are also expected to compensate for the modest light-harvesting capabilities dictated by the lower surface area available for dye anchoring in large-volume nanocrystals.[28]

As of today, realization of the appealing scenarios envisioned for the application of TiO_2 BNCs in DSSCs has been severely hindered by the scarce success met in the elaboration of split nanocrystal architectures through state-of-the-art wet-chemical approaches.[2−4,26] Major synthetic challenges are primarily imposed by the size and shape dependence of the thermodynamic stability order of the possible TiO_2 polymorphs, which is influenced by the chemical potential of solution monomers and ligand-driven modulation of surface energy.[3,26] Further difficulties arise from the fact that anisotropic lattice development and splitting during nanocrystal evolution are mostly governed by competing kinetically controlled processes (e.g., reactant diffusion, facet-specific reactivity, defect formation) under far-from-equilibrium growth regimes.[4,21,26] Such complicated dynamics inevitably restricts the range of experimental conditions under which crystal-phase-controlled BNCs with uniform dimensions and topologies may be preferred over other products. Actually, apart from hierarchical assemblies of primary spherical or needle-shaped particles produced by hydrothermal approaches,[9,10,31] the current library of TiO_2 BNCs remains limited to a few prototypes of split nanostructures, most of which have been obtained in the less desirable rutile phase. These include shuttle-like bundles and polypods derived by slow hydrolysis and aging in acidic media under ambient[32,33] or pressurized conditions,[23,34] chromosome-, star-shaped, and twinned nanorod architectures prepared by thermal decomposition in hot surfactants[24,35,36] or base-catalyzed hydrolysis in mixed aqueous/organic media confined within microchannels,[37] and sawtoothed nanorods obtained by a hydrolytic seeded-growth technique.[17]

Successful exploitation of anisotropic TiO_2 architectures in DSSCs has been achieved with arrays of hierarchical polycrystalline nanostructures characterized by tubular, tree-, or urchin-like habits directly grown on transparent conductive glasses.[29,26,38] In contrast, utilization of colloidal-shaped nanocrystals has been sparsely investigated. Most of the documented cases have dealt with nanorods,[17,18,29,30] whereas the sole few attempts of implementation of BNCs remain restricted to the rutile phase.[17,18] In one earlier report, DSSCs prepared from polydisperse star-like open assemblies of 25 nm × 450 nm nanorod arms were found to attain an energy conversion efficiency as low as $\eta = 2.1\%$.[18] More recently, improved $\eta = 4.3\%$ was claimed for DSSCs assembled from saw-shaped nanostructures individually made of a 20 nm × 150 nm rod-shaped backbone decorated with 4−5 × 20−40 nm branch teeth.[17] However, the relatively modest photovoltaic parameters obtained for such BNC-based cell prototypes indicated electron-transport properties falling below expectations due to possible degradation of the original structural-morphological features of the TiO_2 BNCs and/or introduction of a significant density of charge-recombination centers during film sintering. The difficulty to guarantee safe incorporation of metastable nanocrystals with sophisticated shapes into devices and the yet elusive understanding of the correlation between photoelectrode micro-/nanostructure and inherent electron-transport properties represent major issues retarding full realization of the potential envisioned for BNC-based DSSCs.[28]

In this contribution, we demonstrate a surfactant-assisted nonaqueous sol−gel route that opens access to an unprecedented class of organic-capped TiO_2 BNCs distinguished by a one-dimensional profile and controllable hyperbranched topologies. Our synthetic strategy relies on sequential thermal activation of the aminolysis and pyrolysis reactions of titanium carboxylate complexes in mixtures of oleic acid and oleyl amine at 240−320 °C via a simple multi-injection reactant delivery technique. The sole regulation of the surfactant composition, precursor supply, and temperature enables high-yield production of BNCs selectively trapped in the metastable anatase phase, for which the degree of shape anisotropy and ramification can be modulated over a broad size range (40−200 nm). On the basis of powder X-ray diffraction and high-resolution transmission electron microscopy studies, peculiar structural patterns have been identified to underlie the new TiO_2 architectures, depending on their growth advancement stage. The mechanism of BNC evolution is rationalized within the framework of various thermodynamic and kinetic arguments providing complementary descriptions of the anisotropic crystal-splitting regime realized in the present colloidal system. In addition, we report successful exploitation of the newly developed BNCs in DSSCs. The BNCs have been processed into high-quality thin-film photoelectrodes, in which preservation of the native crystal phase and geometric features of the nanocrystals guarantees a uniform mesoporous structure with effective nanocrystal interconnectivity suitable to maximize light harvesting and electron diffusion. BNC-based DSSCs in standard device configuration (with a conventional N719 dye sensitizer, liquid I^-/I_3^- red-ox electrolyte, and no scattering layer added or $TiCl_4$ treatment applied) indeed afford η approaching 6.2%, which largely overcomes the highest ever achieved for previously documented cells made from wet-chemically prepared and substrate-grown hierarchical TiO_2 nano structures. The photovoltaic performances have been validated by electrochemical impedance spectroscopy analysis, which revealed the genuine impact of the anisotropic split architectures of the BNCs on the ultimate competing balance of charge-transport properties and electron losses due to recombination and trapping events.

2. EXPERIMENTAL SECTION

2.1. Nanocrystal Synthesis. *Materials.* Titanium(IV) chloride ($TiCl_4$, 99.999%), oleic acid ($C_{17}H_{33}CO_2H$ or OLAC, 90%), oleyl amine ($C_{17}H_{33}NH_2$ or OLAM, 70%), 1-octadecene ($C_{18}H_{36}$ or ODE, 90%), anhydrous α-terpineol ($C_{10}H_{18}O$, 99.5%), ethyl cellulose (5−15 mPa·s, 5% in toluene/ethanol 80:20 v/v; degree of ethoxylation: 48%), lithium iodide (LiI, 99.9%), iodine (I_2, 99.99%), and 4-*tert*-butylpyridine (96%) were purchased from Aldrich. 1,2-Dimethyl-3-propyl imidazolium iodide (≥98.0%) was purchased from IoLiTec. AEROXIDE TiO_2 P25 was obtained by Evonik Degussa. Transparent conductive F-doped SnO_2-coated glasses (FTO10−10, 1.1 mm thick, 10 ohm/sq), bis(tetrabutylammonium)-*cis*-di(thiocyanato)-*N*,*N′*-bis(4-carboxylato-4′-carboxylic acid-2,2-bipyridine) ruthenium(II) dye (N719), and Surlyn hot-melt polymer were provided by Solaronix S.A. All solvents used were of analytical grade and purchased from Aldrich. All chemicals and solvents were used as received

Synthesis of Branched TiO_2 Nanocrystals (BNCs). All syntheses were carried out under air-free conditions using a standard Schlenk line setup. Stock reactant solutions of OLAC and $TiCl_4$ were prepared in ODE in a N_2-protected glovebox using previously degassed OLAC and ODE.

As a general synthetic procedure to TiO_2 BNCs, 3 g of ODE, 13 mmol of OLAC, and 1−4 mmol of OLAM were loaded into a three-neck flask and degassed at 120 °C for 45 min, after which the mixture was cooled to 50 °C under N_2 flow. At this point, 1 mL of a 1 M $TiCl_4$ stock solution was added by a disposable syringe, and the flask was heated to 290 °C at a ramp rate of ~20 °C/min. As the temperature was increased, the solution turned from colorless to pale yellow, to dark brown, and finally to white milky. After annealing for 30 min at 290 °C, the reaction could be either halted by removing the heating mantle and allowing natural cooling or continued upon alternating injections (5 mL each) of distinct 0.5 M OLAC and $TiCl_4$ solutions, respectively, at a constant rate of 0.2 mL/min by means of a syringe pump (GENIE Plus Syringe Pump, Kent Scientific). The largest BNCs were obtained by adding up to an additional ~15−18 mmol of both $TiCl_4$ and OLAC to the initial mixture. For the sake of clarity, the nanostructures grown in *single-step syntheses*, namely, after the slow heating and annealing of the starting reaction mixture, are henceforth referred to as *first-generation* BNCs (*I*-BNCs), while those derived upon further growth fed by secondary reactant supply in *multi-injection syntheses* are denoted as *second-generation* BNCs (*II*-BNCs).

The evolution of nanocrystal growth was monitored by analyzing aliquots of the hot surfactant mixture extracted via a glass syringe at scheduled time intervals. The aliquots were suddenly cooled and subjected to TiO_2 extraction procedures, as described below.

Extraction Procedures. After the synthesis, equal volumes of acetone and 2-propanol were added to the crude reaction mixture under ambient atmosphere to induce flocculation of the TiO_2 product, which was then separated upon centrifugation at 5000 rpm and thoroughly washed with acetone to remove reactant residuals. The purified BNCs were dispersible in nonpolar solvents, such as chloroform or toluene, providing optically clear colloidal solutions or stable suspensions, depending on the mean nanocrystal size.

2.2. Fabrication of Dye-Sensitized Solar Cells (DSSCs). *Preparation of TiO_2 Pastes.* TiO_2 pastes suitable for doctor-blade deposition were prepared by purposely modified literature protocols.[30d−f] Two toluene solutions, one containing TiO_2 BNCs (4 wt %/wt) and the other one containing ethylcellulose (10 wt %/wt), were mixed and stirred at 60 °C for 6 h. Then, α-terpineol was added, and the resulting mixture was stirred for an additional 1 h. Finally, toluene was removed by a rotary evaporator. Optimal pastes possessed the following weight percentage composition (determined by gravimetric analysis): TiO_2, 12%; surfactant residuals, 15%; ethylcellulose, 5%; α-terpineol, 68%. For comparison, a Degussa P25-based TiO_2 paste was prepared, as described elsewhere.[39]

Fabrication of DSSC Devices. FTO glasses were first cleaned in a detergent solution using an ultrasonic bath for 15 min and then washed with water and ethanol. Subsequently, the desired TiO_2 paste was deposited onto the FTO substrates (active area: 0.20 cm^2) by the doctor-blade technique and dried at 160 °C for 15 min. This procedure was repeated several times until the desired film thickness was obtained.

To generate TiO_2 thin-film photoelectrodes, the FTO substrates coated with the TiO_2 pastes were subjected to an optimized multistep sintering procedure, which involved gradual heating of the samples under air flow to 160 °C for 10 min, then to 250 °C for 10 min, 360 °C for 10 min, and 480 °C for 30 min. After cooling, the TiO_2 photoelectrodes were immersed into a solution of N719 (0.3 mM) in a mixture of acetonitrile and *tert*-butyl alcohol (1:1 v/v) and incubated at room temperature for 14 h.

DSSC devices were assembled by placing a Pt-coated FTO glass (counter electrode) onto a FTO-supported N719-sensitized TiO_2 photoelectrode (working electrode). The two electrodes were assembled in a sandwich-type cell and sealed with a 50 μm thick Surlyn hot-melt gasket. The red-ox electrolyte, which contained LiI (0.1 M), I_2 (0.05 M), 1,2-dimethyl-3-propylimidazolium iodide (0.6 M), and *tert*-butylpyridine (0.5 M) in dry acetonitrile, was introduced into the inner electrode void space through a hole predrilled on the back of the counter electrode. The holes were sealed up using Surlyn hot-melt film and a cover glass.

2.3. Characterization Techniques. *Inductively Coupled Plasma Atomic Emission Spectroscopy (ICP-AES).* The Ti atomic content in the nanocrystal suspensions/solutions was determined by ICP-AES measurements with a Varian Vista AX spectrometer. The samples for analyses were digested in concentrated HF/HNO_3 (1:1 v/v).

UV−vis Absorption Spectroscopy. The UV−vis absorption spectra of the FTO-supported TiO_2 photoelectrode and of the dye-desorbed solutions were measured with a Varian Cary 5000 UV−vis spectrophotometer.

X-ray Diffraction (XRD). Powder XRD (PXRD) investigations of as-synthesized BNCs were performed with a D8 Discover-Bruker diffractometer equipped with a Cu source, a Goebel mirror, an Eurelian cradle goniometer, and a scintillator detector. PXRD patterns were collected at a fixed incident angle of 3° while moving the detector over the 10−100° range with a step size of 0.05°. Samples were prepared by spreading concentrated solutions of the purified BNCs on top of a silicon substrate. The effect of the thermal treatment on the crystal structure of the BNCs was examined by measuring XRD patterns of sintered BNC-based thin films assembled on Si substrates, following the same procedure used for fabricating FTO-supported photoelectrodes (see below).

The XRD patterns were analyzed by using a whole-profile Rietveld-based fitting program (FULLPROF).[40a] A three-step procedure was applied, as follows. In the first step, the instrumental resolution function (IRF) was evaluated by fitting the XRD pattern of a LaB_6 NIST standard recorded under the same experimental conditions as those used for measuring the samples. The IRF data file was provided separately to the program to allow subsequent refinement of the XRD patterns of the samples. In the second step, the phase composition of the samples was determined by fitting the XRD patterns with the crystal structure models of tetragonal TiO_2 anatase (space group $I41/amd$; cell parameters: $a = b = 3.7835430$ Å and $c = 9.614647$ Å; $\alpha = \beta = \gamma = 90°$) and monoclinic Ti_5O_5 (space group $c2/m$; cell parameters: $a = 5.8006$ Å; $b = 4.1460$ Å; $c = 9.2489$ Å; $\alpha = \gamma = 90°$; $\beta = 107.6°$). The weight percentage accuracy of the estimation was determined to be 5−6% w/w. In the third step, the inhomogeneous peak broadening of the anatase TiO_2 reflections was described by a phenomenological model based on a modified Scherrer formula: $\beta_{h,k,l} = [\lambda/(D_{h,k,l}\cos\theta)] = [\lambda/(\cos\theta)]\,\Sigma_{imp}\, a_{imp}y_{imp}(\theta_h,\Phi_h)$, where $\beta_{h,k,l}$ was the size contribution to the integral width of the (h,k,l) reflection, and y_{imp} were the real spherical harmonics normalized according to a procedure described elsewhere.[40b] After refinement of the a_{imp} coefficients, the program calculated the coherent crystal domain size along each reciprocal lattice vector (h,k,l) direction (note that the IRF broadening dictated an upper limit of about 40 nm for the largest crystal domain size that could be estimated with reasonable accuracy). Other refinable parameters were the unit-cell parameters. The linearly interpolated background was unrefined. The quality of the obtained fits was checked by means of a goodness-of-fit statistical indicator (GoF). GoF values of <3−4 were considered to be satisfactory. The high fit quality and the low GoF indexes proved that the initial assumptions were founded.

Transmission Electron Microscopy (TEM). Low-resolution TEM images were recorded with a Jeol Jem 1011 microscope operating at 100 kV. Phase-contrast high-resolution TEM (HRTEM) and high-angle annular dark-field imaging in scanning TEM mode (HAADF-STEM) experiments were performed using a Jeol 2010F TEM/STEM microscope operating at 200 keV. The objective lens had a spherical aberration coefficient of 0.47 ± 0.01 mm and hence a resolution of 0.19 nm at optimum defocus in HRTEM imaging and of 0.126 nm in STEM imaging, respectively. Samples for analysis were prepared by dropping a dilute toluene solution of freshly prepared BNCs onto carbon-coated copper grids and then allowing the solvent to evaporate. Dynamical multibeam calculations of diffracted intensities were performed by means of a dedicated software (JEMS).[41]

Scanning Electron Microscopy (SEM). The morphology of as-synthesized BNCs prior to sintering and of BNC-based photoelectrodes assembled on FTO substrates was investigated by high-resolution SEM measurements performed with an FEI NOVAnanoSEM200 microscope. Images were typically acquired at an accelerating voltage of 5 kV. Samples of unsintered BNCs for SEM analysis were prepared by UV irradiating a film of freshly synthesized nanocrystals cast on a silicon substrate by means of a He:Hg lamp ($\lambda = 254 \pm 10$ nm; 400 $\mu W/cm^2$) positioned at a distance of 5 cm for 12 h. This treatment led to photocatalytic removal[26] of the insulating organic capping layer at the nanocrystal surface, which otherwise caused significant sample charging, thus hindering SEM image acquisition.

Photoelectrode Thickness Measurements. The thickness of the TiO_2 thin-film photoelectrodes was measured with a Tencor Alpha-Step 500 Surface Profiler.

Dye-Loading Measurements. The amount of N719 adsorbed on the TiO_2 films, henceforth expressed in terms of moles of dye molecules anchored per projected unit area of the photoelectrode, was determined by immersing the sensitized TiO_2 films into a 0.1 M NaOH water/ethanol (1:1 v/v) solution to induce desorption of the dye and then determining the latter spectrophotometrically.[27,28]

Photocurrent−Voltage (I−V) Measurements. Room-temperature $I-V$ curves for the DSSCs were measured using a Keithley unit (model 2400, Source Meter). An AM 1.5 solar simulator (model 91160A, Newport) equipped with a 300 W xenon arc lamp was utilized as the light source. The radiant power was calibrated to 100 mW/cm^2 using a Si solar cell reference. Reproducibility of current measurements was on the order of ≤5%, as checked by measuring three parallel samples for each type of sandwiched photoelectrode structure.

Electrochemical Impedance Spectroscopy (EIS). EIS spectra of the DSSCs were recorded using an AUTOLAB PGSTAT 100 potentiostat operating in two-electrode mode. Measurements were carried out under dark condition at the open-circuit potential by applying an AC voltage of 10 mV in the 300 kHz−30 mHz frequency range. The frequency-dependent EIS curves were fitted using a dedicated software (EC-LAB, BioLOGIC).

3. RESULTS AND DISCUSSION

3.1. Nanocrystal Synthesis and Size/Shape Evolution. Inspired by surfactant-assisted nonaqueous sol−gel routes to oxide nanomaterials,[2,3] we have devised a simple one-pot, multiple-injection strategy by which hydrophobic-coated TiO_2 nanocrystals, distinguished by anisotropic profiles and tunable hyperbranched topologies, can be selectively accessed in the metastable anatase phase over a broad size range. *Single-step syntheses* to *first-generation* BNCs (*I*-BNCs) consisted of the initial slow heating of the $TiCl_4$ precursor in OLAC-rich OLAM/OLAC/ODE media to a target temperature (lying between 240 and 340 °C) under inert atmosphere, followed by prolonged annealing. Once the selected temperature had been reached, TiO_2 generation was typically preceded by a noticeable induction period (∼2−10 min) and manifested through abrupt emergence and fast development of distinct nanostructures with one-dimensional morphologies and variably open-to-close split profiles. The full size of these *I*-BNCs was indeed approached in ∼3−12 min subsequent to nucleation, after which further growth proceeded to a negligible extent on increasing the reaction time. In *multi-injection* syntheses, corresponding sets of *second-generation* nanocrystal derivatives (*II*-BNCs) were obtained upon performing slow alternated additions of calibrated OLAC and $TiCl_4$ amounts, respectively, to the hot reaction environment containing the preformed *I*-BNCs. Upon delivery of extra reactants, the *I*-BNCs progressed toward larger sizes and denser hyperbranched topologies at comparatively slower rate over a subsequent period of

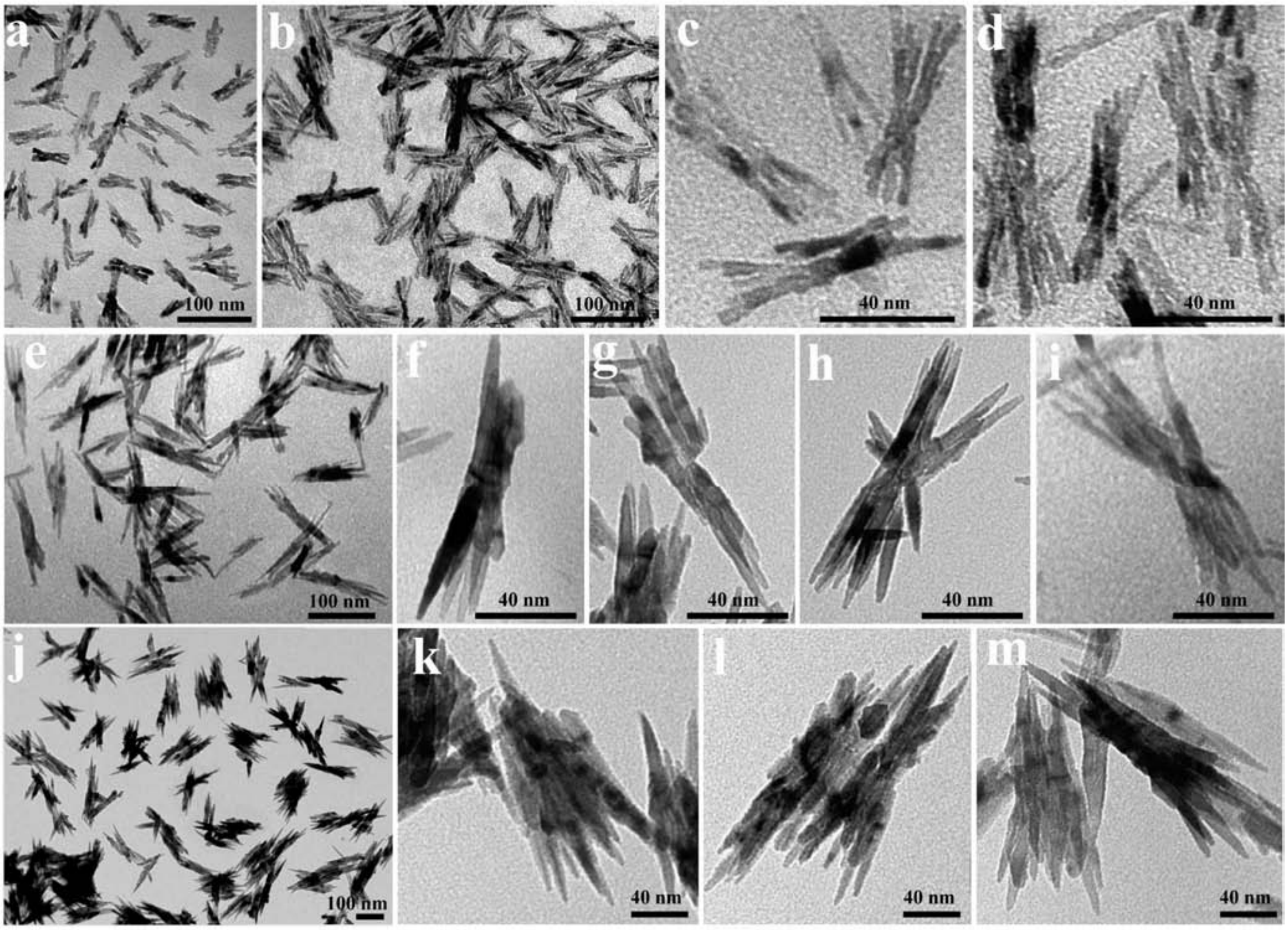

Figure 1. Low-resolution TEM images at variable magnifications of TiO_2 BNCs grown at 320 °C at an initial $TiCl_4$:OLAM molar ratio of 1:4. The panels show: *I*-BNCs obtained in *single-step* synthesis after slow heating and prolonged annealing of the reaction mixture for 5 min (a) and 10 min (b−d) (the prenucleation induction period was ∼3 min) and *II*-BNCs obtained in *multi-injection* synthesis upon slow delivery of extra amounts of both $TiCl_4$ and OLAC reactants to the crude mixture containing the *I*-BNCs: 8 mmol (e−i) and 18 mmol (j−m).

∼1 to ∼6 h. In all circumstances the genuine attainment of lattice-split nanostructures made of permanently interconnected arms (rather than formation of loosely bound aggregates of free-standing shaped nanocrystal subunits) was preliminarily authenticated by the observation that the ramified architecture of the BNCs could withstand repeated extraction/purification cycles of dispersion in nonpolar solvents and alcohol-induced flocculation/centrifugation as well as extensive thermal and/or sonochemical treatments in the liquid phase without being altered or disrupted.

The level of size and shape control enabled by our procedure is illustrated through the representative low-magnification TEM galleries in Figures 1−3, which summarize the outcome of syntheses carried out at different temperatures. In these experiments, the initial reaction mixture in the flask contained fixed $TiCl_4$, OLAC, and ODE amounts, while the OLAM content was varied to accentuate diversification of the BNC morphologies ultimately achievable. The transition from *I*-BNCs to corresponding *II*-BNCs was reproducibly marked by well-correlated size and shape change sequences that depended on the relevant preparation conditions.

Syntheses conducted at 320 °C at an initial $TiCl_4$:OLAM molar ratio of 1:4 (Figure 1) were characterized by the shortest incubation time (∼2−3 min). The reaction resulted in the rapid evolution of delicate cross-shaped and chromosome-like filamentary objects made of a few (4−7) slightly divergent bridged arm segments with diameters and lengths in the 3−4 nm and 70−80 nm intervals, respectively (Figure 1a). The fully developed *I*-BNCs embodied several (10−15) loose-packed nanorod arms configured in one-dimensional, open wheat-sheaf-like assemblies, where the principal subindividual arms appeared to have been tied at their median region and fanned out at their extremities, projecting sizes of up to 15−20 nm transversal to the main elongation direction (Figure 1b−d). The even TEM contrast visible across *I*-BNCs laying with their longer axis parallel to the supporting carbon film suggested that the component arms of the ramified skeleton radiated apart conformal to a roughly planar geometry rather than expanding in all space directions. Corresponding *II*-BNCs derived upon further reactant supply tended to adopt more compact split frameworks that still retained an approximately planar habit. A relatively homogeneous population of single- and double-fantail *II*-BNCs was initially detected (Figure 1e−i). These nanostructures converted to a broadly shape-spread family of complex asymmetrically split objects, including mono- and polybundle architectures arranged in T-, V-, and X-like acicular geometries (Figure 1j−m), in which

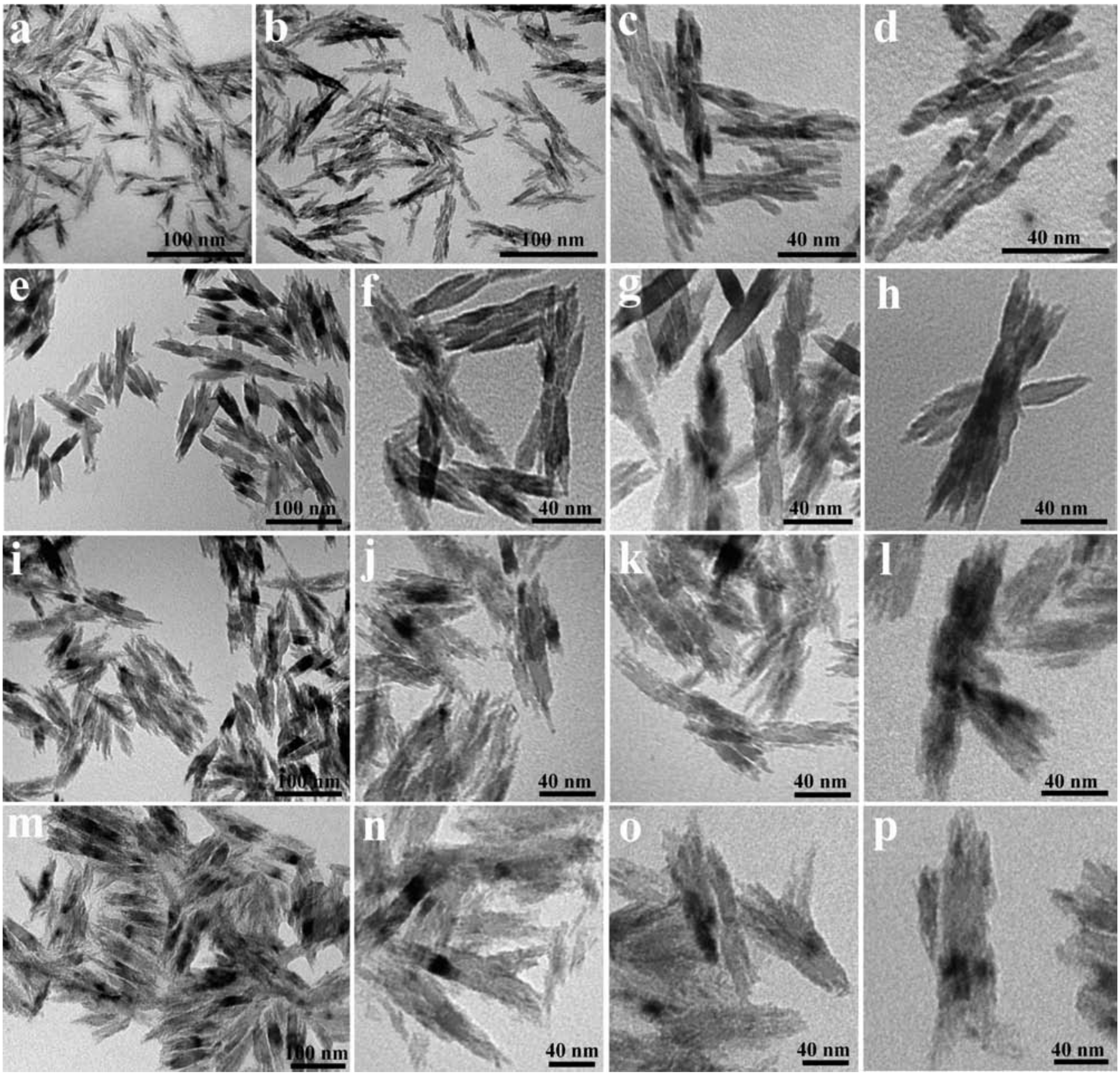

Figure 2. Low-resolution TEM at variable magnifications of TiO_2 BNCs grown at 280 °C at an initial $TiCl_4$:OLAM molar ratio of 1:2. The panels show: *I*-BNCs prepared by *single-step* synthesis after slow heating and prolonged annealing of the reaction mixture for 8 min (a) and 12 min (b−d) (the prenucleation induction period was ~6 min) and *II*-BNCs obtained by *multi-injection* synthesis upon slow delivery of extra $TiCl_4$ and OLAC reactants to the crude mixture containing the *I*-BNCs: 8 mmol (e−h), 12 mmol (i−l), and 18 mmol (m−p).

each bunch subunit originating from the same core region embodied numerous (8−12) parallel or slightly divergent arms with thickness and length of up to 6−8 nm × 180−200 nm, respectively.

In syntheses performed at 280 °C at a $TiCl_4$:OLAM molar ratio of 1:2 (Figure 2), TiO_2 nucleation was delayed to a comparatively longer extent (5−6 min). The reaction led to evolution of *I*-BNCs exhibiting constrained topologies that individually assembled several (7−10) tight-packed 4−6 nm × 70−80 nm nanorod arms into parallel and slightly fanning-out bundles (Figure 2a−d). Upon sustaining growth with secondary precursor additions, these *I*-BNCs converted to a population of larger *II*-BNCs, which was dominated by oblate and single-/double-ponytail objects bearing toothed terminations and included a minority of half-opening sheaf-like objects (Figure 2e−h). As their short and long axes systematically enlarged over the 30−50 nm and 130−200 nm intervals, respectively, the *II*-BNCs acquired tight-split topologies distinguished by a remarkably enhanced projected solidity, across which the overlapping of the main thick arms often attributed to a braid-type fringe contrast variation. On approaching their upper size limit, the hyperbranched nanostructures developed irregularly faceted longitudinal sidewalls and densely indented apexes (Figure 2i−p).

Finally, syntheses performed at 240 °C, the minimum temperature at which TiO_2 formation could be triggered, were examined. In line with previous findings, the prenucleation induction stage extended even further (up to 8−10 min) under these conditions. At an initial $TiCl_4$:OLAM molar ratio of 1:1,

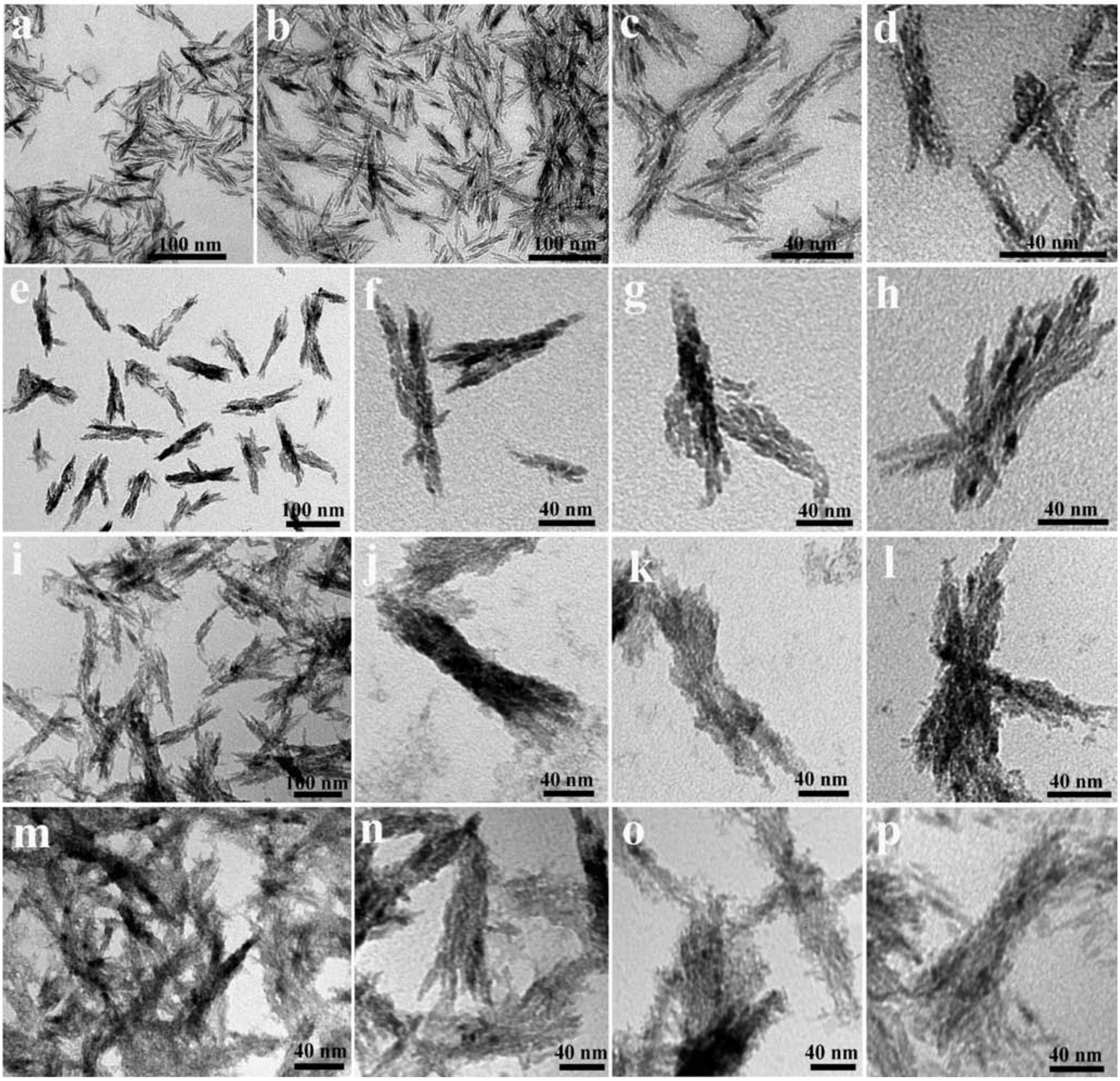

Figure 3. Low-resolution TEM at variable magnifications of TiO_2 BNCs grown at 240 °C at an initial $TiCl_4$:OLAM molar ratio of 1:1. The panels show: *I*-BNCs obtained in *single-step* synthesis after slow heating and prolonged annealing of the reaction mixture for 12 min (a) and 15 min (b−d) (the prenucleation induction period was ∼10 min) and *II*-BNCs obtained in *multi-injection* synthesis upon slow delivery of extra amounts of both $TiCl_4$ and OLAC reactants to the crude mixture containing the *I*-BNCs: 8 mmol (e−h), 12 mmol (i−l), and 18 mmol (m−p).

the reaction yielded *I*-BNCs with highly split bunch-shaped profiles, which bandaged several thin filaments that, in turn, split apart along their elongation direction and accommodated much shorter secondary arms of dissimilar lengths (Figure 3a−d). On supply of further reactant feedstock, the tendency toward branching was exacerbated. The resulting *II*-BNCs adopted densely filamentous sheaf-like architectures often exposing asymmetric half-fantails (Figure 3e−l), which ultimately tended to aggregate or fuse into intricate three-dimensional network superstructures (Figure 3m−p).

3.2. Nanocrystal Characterization. A detailed insight into the compositional and structural identity of the BNCs was gained through combining PXRD analyses of dry powder samples with STEM-HAADF and HRTEM investigations of individual nanocrystals. To illustrate the most distinctive features of the newly developed split topologies, Figures 4−6 summarize the characterization results pertinent to typical sheaf-like *I*-BNCs and bundle-based *II*-BNCs thereof with overall projected short-/long-axis dimensions of 10−15 nm × 70−80 nm and 20−25 nm × 120−130 nm, respectively, as representative cases of study of branching and anisotropic lattice evolution in different synthesis stages.

The experimental PXRD patterns of the BNCs indicated the formation of the nanometer-scale crystalline domains of the

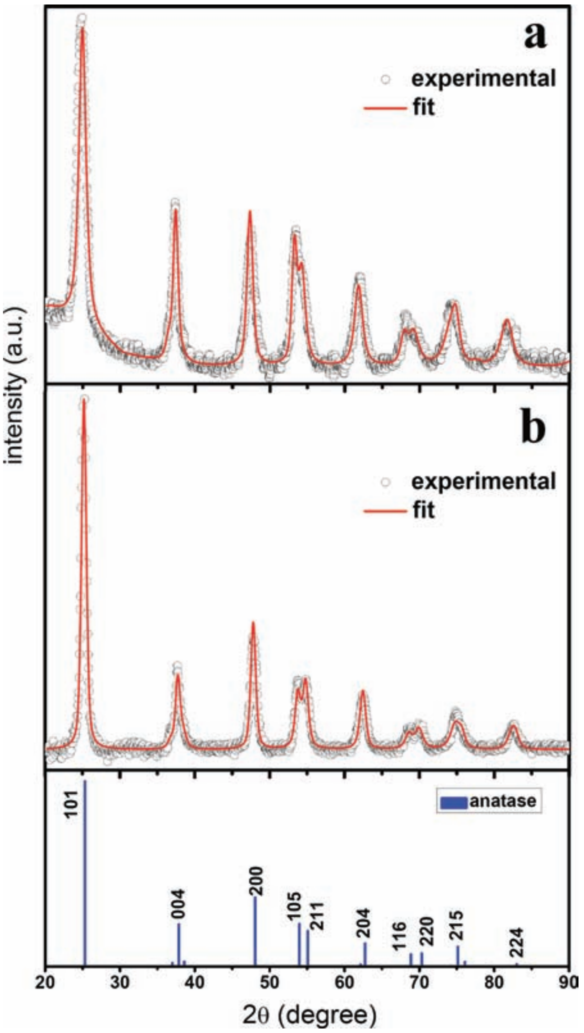

Figure 4. Representative PXRD patterns of *I*-BNCs with overall projected dimensions of 10−15 nm × 70−80 nm (a) and thereof derived *II*-BNCs of 20−25 nm × 120−130 nm (b), along with the reference pattern of bulk TiO_2 anatase. The experimental curves (dotted lines) are compared to the corresponding Rietveld-based fits (continuous lines). The refined cell parameters were calculated as follows: $a = b = 0.384$ nm, $c = 0.962$ nm for *I*-BNCs and $a = b = 0.380$ nm, $c = 0.953$ nm for *II*-BNCs, respectively. Any possible contamination by other phases (e.g., Ti_5O_5) should be below 5−7% w/w, i.e., the accuracy of the fitting procedure. The GOF indicators were <2 in both cases.

anatase TiO_2 polymorph. Quantitative phase analysis of the data by means of our Rietveld-based approach[40] confirmed the substantial phase purity of the samples with an accuracy of ≤5−6% w/w (Figure 4). Calculation of the refined structure parameters evidenced that the anatase unit cell volume of the BNCs subtly deviated from that of the corresponding TiO_2 bulk material ($I4_1/amd$ tetragonal space group with $a = b = 0.378$ nm and $c = 0.951$ nm) by about 4.4% in the *I*-BNCs and by 1.3% in the *II*-BNCs sample due to lattice expansion along all crystallographic axes ($a = b = 0.384$ nm, $c = 0.962$ nm and $a = b = 0.380$ nm, $c = 0.953$ nm, in the respective cases). Similar structural distortions have been frequently assessed in TiO_2 nanomaterials on the basis of elaborate Rietveld analyses of X-ray and electron diffraction data and assumed to originate from nonstoichiometry and/or strain effects.[26,42]

The PXRD profile of the *I*-BNCs (Figure 4a) diverged from the bulk anatase reference pattern by the inhomogeneous line broadening and noticeable alterations in the relative intensities of the various reflections, among which the (002) and, especially, the (004) were distinguished by their extreme prominence and sharpness. Because of the random orientation of nanocrystals in their corresponding dry powder samples, the observed spectral features preliminarily authenticated existence of crystalline domains anisotropically extended along the equivalent *a*-/*b*-axes and the *c*-axis of the anatase lattice, the latter being the preferential elongation direction.[26] By comparison, the spectral signature of nanocrystal shape anisotropy was less accentuated in the PXRD pattern of the braid-shaped *II*-BNCs because of the generally narrower and better resolved reflections associated with the formation of larger domain sizes (Figure 4b).

The coherent crystal domain size along the relevant *hkl* crystallographic orientations, $D_{[hkl]}$, was estimated accounting for the inhomogeneous line broadening in the patterns by means of a phenomenological model based on a modified Scherrer formula[40] (see Experimental Section). The calculations confirmed that the anatase lattice had indeed developed the most along the *c*-axis, far exceeding the extension threshold beyond which the IRF prevented accurate size estimation (i.e., $D_{[004]} >$ 40 nm). This result was consistent with the average length of the nanorod subcomponents measured by low-resolution TEM. In addition, the mean crystal domain size along the four equivalent [200]/[020]-type directions was determined to be remarkably larger than those along the eight equivalent [101]/[011]-type orientations ($D_{[200]/[020]} = \sim 17$ nm/∼35 nm and $D_{[101]/[011]} = \sim 7$ nm/∼15 nm for the respective samples of *I*-BNCs and *II*-BNCs selected). These findings discredited the hypothesis that the BNCs could be merely composed of multidomain bunches of physically interacting (e.g., through electrostatic forces) monocrystalline *c*-axis-elongated nanorod constituents with even diameter. In fact, for powders of such loosely bound nanorod assemblies, $D_{[200]/[020]}$ approximating the TEM-measured diameter (3−5 nm and 5−8 nm for *I*-BNCs and *II*-BNCs, respectively) and $D_{[101]/[011]} > D_{[200]/[020]}$ should be instead expected.[26,35,36,43,44] Rather, the domain size peculiarities inferred from PXRD analyses preliminarily suggested that the BNCs possessed an anisotropically shaped lattice split skeleton, in which the bandaged nanorod subcomponents should be epitaxially fused, thereby attaining crystal extension orthogonally to the main *c*-axis elongation direction of the BNCs (i.e., along the *a*-/*b*-axis orientations).

Figure 5 shows representative STEM-HAADF and HRTEM studies of typical sheaf-like *I*-BNCs. The HAADF images (Figure 5a−d), where the brightness is related to the local crystal thickness and to average atomic number, confirmed the unique branched topologies previously inferred from low-resolution TEM inspection (Figures 1−3). The BNCs indeed appeared as one-dimensional split nanostructures made of several twisted arms with relatively uniform diameter, which were bandaged or fused at their median region, forming roughly planar fantails (Figure 5a). Interestingly, detailed inspection at higher magnification (Figure 5b−c) revealed that most *I*-BNCs were randomly decorated with multiple polydisperse spherical particles that exhibited a much brighter HAADF contrast in spite of their tiny sizes (1.5−4 nm). This fact indicated that such contaminating clusters should be composed of a Ti-containing phase characterized by a heavier mean atomic number than the majority anatase TiO_2 of which the branched skeleton was made (see next paragraphs).

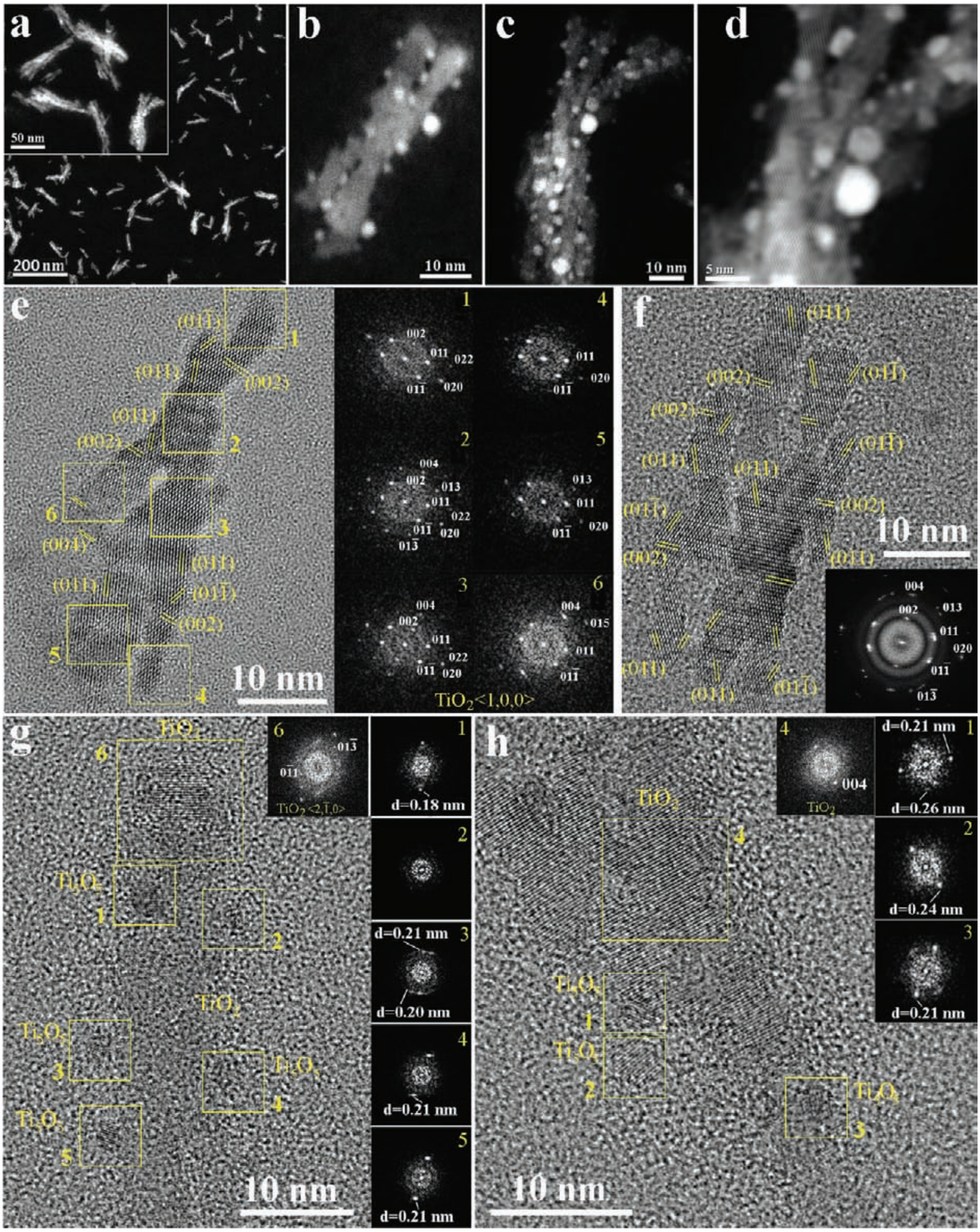

Figure 5. Representative characterization studies of individual *I*-BNCs. The panels show: (a−c) Low- and (d) high-resolution STEM-HAADF images of sheaf-like *I*-BNCs, showing decoration of the main branched body by clusters with a heavier mean atomic number; (e) HRTEM image of an asymmetric fork-shaped *I*-BNC viewed down the ⟨100⟩ zone axis (left), along with the FFTs calculated from the corresponding labeled regions enclosed by yellow boxes (right); (f) HRTEM image of a *I*-BNC made of a central chromosome-like skeleton with one extra arm attached to the left side, viewed down the ⟨100⟩ (left). The FFT calculated for the entire nanostructure is reported in the bottom right inset. (g, h) Examples of *I*-BNCs captured under orientations that disclose the presence of small Ti_5O_5 domains on their surface. The FFTs calculated from the respective numbered regions marked by yellow boxes are also shown.

High-resolution HAADF imaging (Figure 5d) disclosed fringe continuity across the whole skeleton of the *I*-BNCs and the monocrystalline nature of the foreign domains, suggesting that the latter matched crystallographically with the supporting lattice underneath. Note that, because contrast in the bright-field TEM imaging mode is mostly dictated by electron diffraction conditions and specimen thickness rather than by average atomic number effects, the decorating clusters were detectable by low-resolution TEM inspection only rarely (cf. Figures 1−3 and Figure S1 in the Supporting Information)

HRTEM investigations, supported by fast Fourier transform (FFT) analysis of the relevant images, provided an accurate insight into the intricate structure of the *I*-BNCs. Two typical cases of study, which clarify the distinguishable architectural motifs underlying both anisotropic lattice development and branching, are reported: the first example refers to a *I*-BNC with an asymmetric fork-like projected shape (Figure 5e), while the second one concerns a *I*-BNC built up of a central chromosome-like body with one additional longitudinal arm attached aside (Figure 5f). On the basis of the calculated FFTs, the *I*-BNC structure could safely be interpreted as monocrystalline anatase TiO_2 down its ⟨100⟩ zone axis. The main constituent branches of the *I*-BNCs were [001]-elongated domains with diameters and lengths of 3−5 nm and 30−50 nm, respectively, which exposed stepped longitudinal sidewalls made of crystallographically equivalent (011)/(101)-type facets and terminated with (001)-type facets at their apexes. Analogous structural arrangements have been reported for a variety of colloidal rod-/wire-shaped TiO_2 micro- and nanostructures, grown in solution phase, for example, by oriented attachment mechanisms or under assistance of organic stabilizers capable of facet-preferential adhesion.[2,26] Formally, ramifications were attained when several parallel arms were partially interconnected along the [100]/[010] (i.e., along the *a*-/*b*-axes, orthogonal to the *c*-axis) and/or transversally along [011]/[101] directions (at 63.8° relative to the *c*-axis) through corresponding bridging sections and consequent elimination of (011)/(101)-type facets from the sidewall locations at which junctions were created[35] (Figure 5e,f). The relevant branch points were randomly distributed across the *I*-BNC skeleton, however preferentially concentrating at the median region of the sheaf-like body, where the component filaments actually appeared to have been bandaged in low-magnification TEM images (cf. Figures 1−3). Within the detection limits of the HRTEM investigation, no defects were identified in proximity of the ramifications. Overall, the deciphered lattice splitting pattern guaranteed crystal continuity across the *I*-BNC skeleton, accounting for the existence of crystalline domains that extended dominantly along the [001] and moderately along the [100]/[010] (i.e., along the *a*-/*b*-axes) and/or the [011]/[101] directions (at 63.8° relative to the *c*-axis). This result matched with the complex crystallographic-direction dependence of the $D_{[hkl]}$ values deduced from the PXRD data.

As another interesting aspect deserving remark, the HRTEM images of the above *I*-BNCs were characterized by a complicated spatial distribution of the projected phase contrast. To interpret the relevant profiles, FFTs were derived from different regions along the *I*-BNC body and compared with corresponding simulated diffractograms obtained by dynamical multibeam calculation of the diffracted intensities as a function of the sample thickness (Figure S2 in the Supporting Information). The results of this analytical study applied to the first selected case of *I*-BNC (Figure 5e) can be used to highlight the significance of subtly varying HRTEM contrast features across the projected nanostructure lattice. For the considered nanocrystal, only the FFT corresponding to the area marked as "4" matched almost perfectly with anatase viewed along the ⟨100⟩ zone axis. Interestingly, the FFTs relative to the sections labeled as "1", "2", and "3" evidenced emergence of the (002) reflections that are prohibited for the $I4_1/amd$ tetragonal space group under kinematical scattering conditions.[45] The simulations clarified that possible local variations in the crystal lattice thickness (up to ∼10 nm) did not suffice to account for the observed contrast changes (Figure S2 in the Supporting Information). For instance, given the thinness of section "1" (only ∼4 nm), the enhanced visibility of the (002) spots could not arise from multiple electron scattering events. In addition, the (011) reflections were always stronger than the (01−3) ones, whereas the simulation predicted them to exhibit comparable intensities across the thickest regions denoted as "2" and "3" (for the latter area, the experimental diffractogram displayed nearly invisible (01−3) spots). Finally, the image contrast in the regions "5" and "6" could, at least partly, result from a tilt of the relevant branches about a direction normal to the supporting grid plane. Similar discrepancies emerged from the detailed FFT analysis of the second example of *I*-BNC reported in the figure (Figure 5f). In the latter case, the presence of single oblate as well as split reflections in the global FFT pattern of the entire nanostructure (Figure 5f, bottom right inset) clearly highlighted that some portions of the branches were appreciably twisted relative to the central part of the nanostructure (for example, the maximum value of twist in the (100) plane, as measured from the FFT, was about 8°). Unusual diffractograms characterized by anomalous diffracted intensities and kinematically forbidden reflections, not otherwise explainable on the basis of sample thickness effects, can correlate with minute deviations of the anatase crystal structure from that of the bulk counterpart, as recently demonstrated in the investigations of analogous surfactant-capped TiO_2 nanocrystals by means of a combined technique of HRTEM and electron diffractive imaging.[45] Possible causes of such divergence include alterations in atomic occupancy and lattice distortion due to nonnegligible surface strain, modified unit cell geometry, and nonstoichiometry.[26,42,45] Therefore, the small dilatation of the anatase lattice parameters inferred from PXRD data analyses could reasonably be assumed to be at the origin of the particular HRTEM features detected for the present *I*-BNCs. It is plausible to assume that the joint effects of the expanded anatase lattice, on one side, and of the slightly distorted geometry to which interconnected rod-shaped branch sections are constrained, on the other side, can determine insurgence of appreciable strain fields propagating across individual *I*-BNCs.

HRTEM imaging of other *I*-BNCs suitably aligned down different zone axes allowed identification of multiple tiny clusters that randomly functionalized the main TiO_2 anatase branched skeleton (Figure 5g,h). The lattice fringe spacings of the foreign domains measured by the FFT analysis matched well with those of the monoclinic Ti_5O_5 phase (space group $c2/m$; a = 0.58553 nm, b = 0.93405 nm, c = 0.41422 nm, β = 90° in unique *b*-axis configuration).[46] On the basis of this finding, the small bright particles that appeared to decorate the *I*-BNCs in the relevant HAADF images could be reasonably attributed to Ti_5O_5 due to its higher average atomic number relative to TiO_2 (cf. Figure 5a−d). Occasionally, other types of $TiO_2-Ti_5O_5$ nanocrystal heterostructures, which had not evolved into branched objects, were detected (Figure S3 in the Supporting Information), suggesting the Ti_5O_5 might be generated in different stages of the formation of *I*-BNCs. To our best knowledge, this is the first time that monoclinic Ti_5O_5 has been obtained via a liquid-phase route.[46] The absence of any clear Ti_5O_5 signature in the PXRD

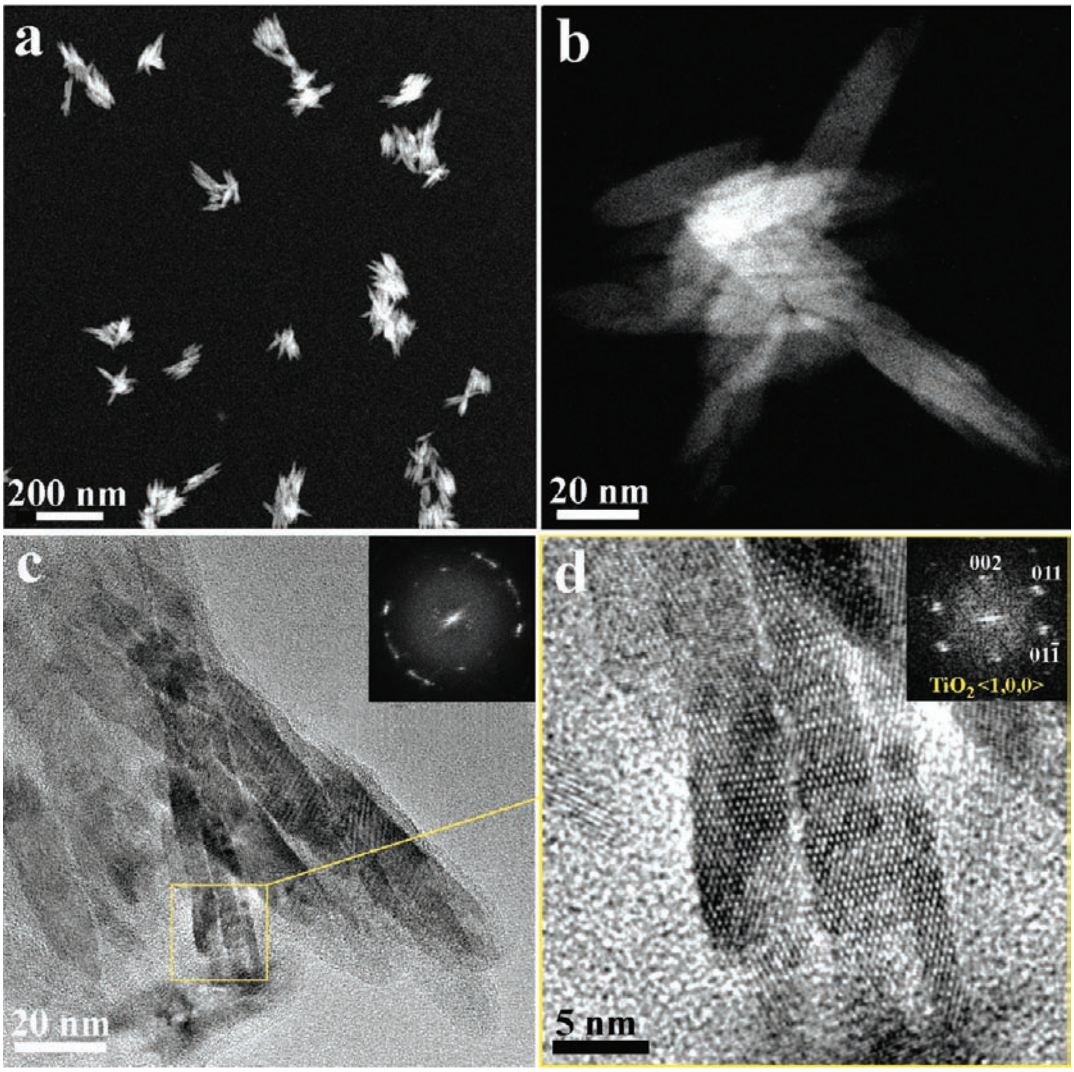

Figure 6. Representative characterization studies of individual *II*-BNCs. The panels show: (a,b) Variable-magnification, low-resolution STEM-HAADF images of multibundle *II*-BNCs with uniform composition; (c) HRTEM image of a large portion of a single I-BNC that bears arms partially aligned around a common axis parallel to the [100]. The relevant FFT is reported in the top right inset. (d) A magnified view of the region enclosed by a yellow box in panel c, which captures the terminal sections of two arms that are rotated relative to each other by about 6° around the [100]. The corresponding FFT is reported in the top right inset.

patterns could be easily explained by considering the low percentage content of this phase (≤5−6% w/w, i.e., the accuracy of the data fitting procedure), its intrinsically low X-ray scattering power, the large peak widths associated with the small cluster sizes, and the considerable superimposition of many Ti_5O_5 and anatase TiO_2 reflections (Figure S4 in the Supporting Information).

Figure 6 illustrates the structural details pertinent to a representative sample of larger multibundle-shaped *II*-BNCs. The nanostructures incorporated variously oriented bundles, each made of 5−8 nm thick arms that reached lengths of up to 150−170 nm. The HAADF inspection (Figure 6a,b) evidenced the characteristic braid-like profile of the individual bunch subcomponents of the nanostructures, along which brightness changes were caused by obvious thickness variations due to overlapping arms. No evidence for the presence of foreign clusters of Ti_5O_5 or other phases contaminating the TiO_2 anatase skeleton was found. The HRTEM image of a *II*-BNC viewed down the ⟨100⟩ zone axis (Figure 6c) showed a characteristic phase-contrast profile with distinguished Moiré fringes arising from the superimposition of several arm filaments. The FFT of the whole object exhibited a textured ring pattern (top right inset in Figure 6c) that disclosed the peculiar spatial organization of the nanostructure, where several sub-bundles, each grouping a few roughly parallel *c*-axis-elongated TiO_2 anatase arms, were partially arranged around a common [100] direction. This fact could be better appreciated by observing that the FFT relative to a selected nanostructure portion enclosing the terminal sections of two neighboring arms (top right inset in Figure 6d) displayed double-spot reflections because the concerned rod sections were rotated around the [100] by about 6° with respect to each other. As previously discussed, the visibility of the kinematically forbidden (002) reflections highlighted existence of an inherently distorted anatase unit cell structure. Unfortunately, any further insight into the structure of the splitting junctions was hindered by the large thickness and/or complex image contrast that featured the relevant crossover regions due to partial arm overlapping. However, the PXRD analyses suggested that the nanostructure lattice had coherently expanded to a significant extent not only along [001], in agreement with the observation of the monocrystalline domains of the longer arms, but also along the *a*-/*b*-axis directions (Figure 4b).

3.3. Growth Mechanism. The present TiO_2 BNCs with controllable hyperbranched topologies and tunable geometric parameters result from a nonhydrolytic route that involves programmed thermal activation of a suitably composed reaction mixture, in combination with controlled secondary injections of selected reactants. This synthesis scheme enables a convenient dynamics of delayed nucleation and fast-growth processes, across which formation and stabilization of the metastable anatase phase over a broad size range, lattice splitting, and anisotropic development of the evolving nanocrystals depend on a complex interplay of thermodynamic factors and kinetic processes. These mechanisms are discussed in detail as follows.

3.3.1. Size and Shape Evolution. Monitoring of the reaction progress clarified that *I*-BNCs with already clearly developed bundle to sheaf-like topologies were detected suddenly after an induction period subsequent to the slow heating of the initial mixture to the selected reaction temperature. Although the exceedingly fast growth rate prohibited capturing the system in the early evolution stages close to nucleation, the shape symmetry and size homogeneity of the nanocrystals forming in single-step syntheses suggested that the *I*-BNCs derived upon direct lattice splitting of corresponding primordial seeds, followed by parallel development of multiple filament arms along diametrically opposed fanning-out directions.[2,4a,23,25] (cf. panels a−d in Figures 1−3). In multi-injection synthesis, further anisotropic growth sustained by extra reactant supply was accompanied by implantation of additional branches onto the median regions of the nanostructures and, yet less frequently, onto the pre-existent primary arms. This ultimately led to *II*-BNCs with more complex dense-split topologies and variable degrees of symmetry (Figures 1−3). The fact that the sample population was dominated by branched objects with uniform features, which grew to progressively large volumes over the entire synthesis course, discredited the hypothesis that the BNCs formed via crystal-oriented attachment or directional etching/recrystallization of primordial solid particles that could have been produced in the earlier stages. In fact, if such pathways had been operative, the relative fraction of BNCs should have gradually increased over time at the expense of other particle types within the sample.[2,4,6,12,13b,14] However, no transitions in support of any of the aforementioned mechanisms were detected.

Taken together, our findings allowed concluding that the BNCs evolved through a steady-growth process that proceeded at the expense of the reactive atomic/molecular species (monomers) available in the solution environment. The *I*-BNCs originated from a single homogeneous nucleation event and a subsequent time-limited *primary branching* stage that involved concerted arm growth out of the initially generated seeds. If fed with extra reactant supply, the *I*-BNCs progressed to larger hyperbranched *II*-BNCs as a result of *secondary splitting* events and continuous anisotropic branch development.

3.3.2. Chemical Pathways Underlying TiO_2 Formation. It has been established that, during heating of $TiCl_4$/OLAC/OLAM mixtures (at $T > 230$ °C) TiO_2 nucleation and growth are driven by condensation of (poly)titanium hydroxo/oxo molecular species, which indeed represent the actual monomer units for building the oxide lattice. Such intermediates can evolve from two main pathways, namely: (i) OLAM-driven aminolysis of in situ generated titanium (amino) chloride oleate complexes (henceforth, simply referred to as Ti-OLAC), in which OLAM is progressively consumed upon nucleophilic attack to carbonyl carbon atoms and released as oleyl amide byproduct, and (ii) direct thermal pyrolysis of Ti-OLAC.[2,3,4a,44,47] Since the two reactions are characterized relatively high, yet have dissimilar energy activation barriers,[44,47,48] release of the respective monomers into the solution can take place at distinct slow rates and/or temperatures. Profiting from this knowledge, we have realized an appropriate temporal modulation of the liquid environment composition that allows exploitation of the aminolysis and pyrolysis reactions in selected stages of the synthesis course, thereby achieving convenient time separation of the fundamental nucleation and growth processes.

The production of the *I*-BNCs in single-step syntheses, which relied on the heating of the $TiCl_4$ precursor in OLAC-rich OLAC/OLAM mixed media, was dominantly sustained by monomers provided by the more kinetically favored Ti-OLAC aminolysis route. As a consequence of the slow monomer accumulation, the nucleation event was significantly delayed, relative to the nominal precursor injection step.[47,48] The pre-nucleation induction period (2−10 min) shortened at increasingly higher temperatures and OLAM content. In the limiting case of OLAM-free preparations, no TiO_2 generation was detectable over the typical running time of single-step synthesis, confirming that Ti-OLAC pyrolysis pathways were comparatively more hindered, as previously assessed.[47] These facts indicated that the progress of the aminolysis reaction indeed dictated the rate at which the critical supersaturation threshold necessary for surpassing the huge energy barrier for homogeneous nucleation was crossed (hence, the extension of the incubation time).[2,48] The nucleation manifested as a sudden burst-like event that self-quenched as the supersaturation degree was quickly relieved.[48] Subsequent diffusion-controlled growth of the as-generated seeds to *I*-BNCs occurred in an OLAM-depleted environment at an exceptionally high rate (with the maximum *I*-BNC size being reached in 3−10 min after nucleation), which suggested an autocatalytic growth process, due, for example, to acceleration of the aminolysis and/or monomer condensation reactions at the surface of the evolving nanocrystals.[47,48] The capability of OLAM to simultaneously act as effective reductant at high temperature may explain the transient observation of a minor fraction of the uncommon reduced titanium-oxide phase, Ti_5O_5, in this synthesis stage. On the other hand, the contribution from the slower pyrolysis pathways can be assumed to be negligible due to the scarce availability of unreacted Ti-OLAC species after the aminolysis, as expected on the basis of reactant stoichiometry (1:1 < Ti:OLAM < 1:4). These attributions are consistent with the fact that the purified *I*-BNCs ultimately retained a dominant OLAM capping at their surface (Figure S5 in the Supporting Information).

Notably, the degree of branching and skeleton densification of the *I*-BNCs was accentuated upon decreasing the OLAM content and reaction temperature. Such dependence can be understood on considering that the moderate supersaturation levels determined by these conditions should lead to reduced monomer consumption in the nucleation process and, consequently, to generation of fewer crystal embryos. The latter had to compete less with each other for the proportionally larger amount of remaining monomers, thus allowing development of nanocrystals with a higher number of arms.[2,25] A large availability of reactive species per generated seed is known to be a general prerequisite to propelling branching out and sustaining anisotropic arm growth.[2,4,49]

By comparison, the *II*-BNCs produced in multi-injection syntheses were derived from their parent *I*-BNCs upon supply of monomers originating from the more kinetically hindered pyrolysis of Ti-OLAC complexes that were slowly replenished upon reiterated $TiCl_4$ and OLAC additions. In these circumstances, the even modest extent of the decomposition reaction guaranteed a monomer concentration sufficient to narrowly overcome the much lower activation barrier for *secondary branching* events and growth continuation of the pre-existing arms.[2,4,48] The *I*-BNCs thus evolved to increasingly branched *II*-BNCs with longer and equally thick arms over a period of 1−6 h, hence at a comparatively reduced rate than in the previous synthesis stage, while induction of parasitic homogeneous nucleation was eluded because the solution supersaturation maintained at a constantly moderate level. The dominant contribution of the pyrolysis reaction to TiO_2 growth agrees with the observation that the final *II*-BNCs accommodated a surface capping layer made of oleate anion ligands (Figure S5 in the Supporting Information).

To summarize, the nonhydrolytic synthesis technique of programmed precursor/surfactant delivery devised by us guaranteed an appropriately balanced utilization of monomers in the fundamental stages of nanocrystal formation. The aminolysis pathways acted as the faster monomer-generating route that allowed triggering nucleation and promoted rapid growth of *I*-BNCs with variable degrees of branching, depending on the relative seed to monomer ratio attained. The pyrolysis pathways sustained slower conversion of well-developed *I*-BNCs to increasingly large *II*-BNCs, keeping the established shape evolution regime essentially invariant. Overall, since the reactive species which contributed to nucleation and earlier growth were distinct from those involved in later development, and these processes showed dissimilar monomer concentration dependence, they did not overlap in time. The appropriate balance of monomer generation and utilization across the nucleation and growth stages, which was ultimately realized, explains the flexibility with which uniform BNCs were achieved with tunable dimensions and variably branched topologies.

3.3.3. Mechanism of Branching and Anisotropic Growth. The complex shape evolution of the present BNCs can be rationalized on the basis of different mechanistic arguments providing complementary descriptions of branching and anisotropic development. We propose that BNCs result from a growth regime where thermodynamic pathways, related to the crystal-structure-directing effect of the initially nucleated seeds and the free surface energy changes accompanying shaping, interplay with kinetically controlled processes associated with diffusion-limited monomer fluxes and surfactant-induced stabilization of the metastable anatase lattice.

a. Role of Crystal Structure. As a primary condition predisposing to anisotropic shaping, it should be considered that the anatase polymorph, in which the BNCs are stabilized under the present solution environment, offers a structural basis inherently suitable to underlie both anisotropic growth and branching.[2] Scheme 1 illustrates that, at the molecular level, the anatase may indeed be visualized as being composed of predominantly edge-sharing distorted TiO_6 octahedrons (where each Ti^{4+} cation is coordinated to six O^{2-} ions) which are arranged in *cis*-screwed ribbons twisting around the *c*-axis. Each TiO_6 unit is condensed to four other neighbors through two adjacent O^{2-} edges in the *bc*-plane and two edges in the *ac*-plane, respectively.[26] The inherent anisotropy (tetragonal unit cell) and centrosymmetry (body-centered lattice) of anatase TiO_2 can promote equidirectional linear development of the nanocrystal lattice either along or perpendicular to the unique *c*-axis of high symmetry.[2,26] In addition, because of the TiO_6-based chain-like pattern, the lattice can potentially expand out of the main *c*-axis stem in any of the other alternating *zig-zag* directions along which the component TiO_6 blocks are interlaced, eventually leading to branching along

Scheme 1. Atomistic Representation of Anatase TiO_2 Lattice (The Relevant Unit Cell and Crystallographic Directions Are Also Marked for the Sake of Clarity)[a]

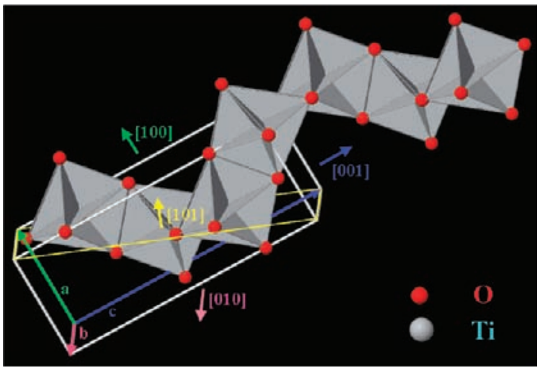

[a] The structure can be visualized in terms of *ziz-zag* ribbons of condensed edge-sharing TiO_6 octahedral units, which individually comprise one Ti^{4+} ion at the center, coordinated to six peripheral O^{2-} ions.

Scheme 2. Simplified Representation of the Structural Pattern Underlying *Primary Branching* and Anisotropic Arm Development in *I*-BNCs[a]

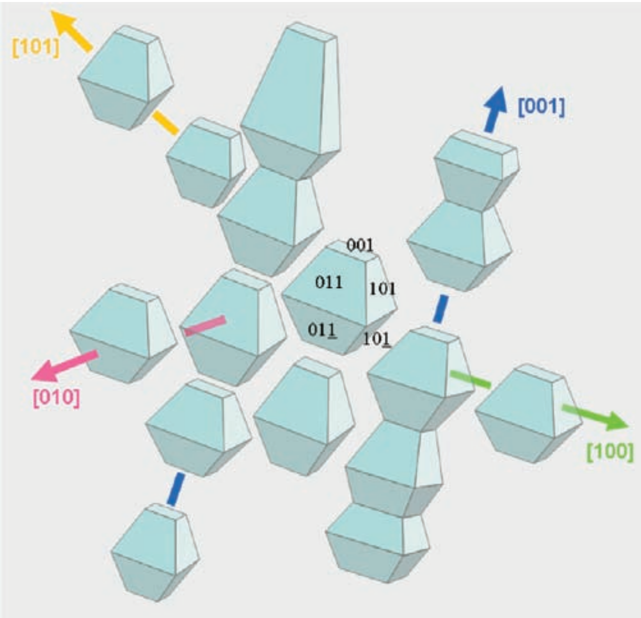

[a] The monocrystalline split skeleton can formally be decoupled into irregularly stretched, truncated octahedral bipyramidal units with variable sizes, which are interconnected most frequently along the [001] and partially along the [010]/[100] and [101]/[011] directions, leading to arms and branch regions, respectively (cf. Figure 5e,f).

Scheme 3. Proposed Mechanism of *Secondary Branching* and Arm Development in *II*-BNCs[a]

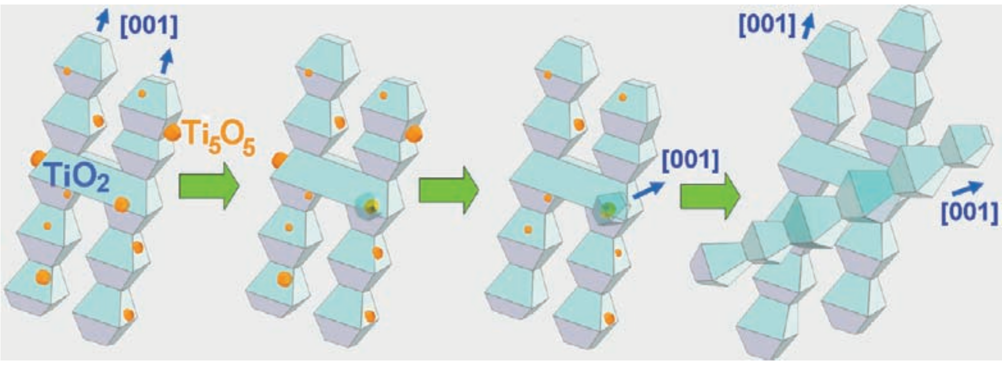

[a] Critical-size Ti_5O_5 domains formed on the monocrystalline *I*-BNCs (here, an early grown *I*-BNC with only two arms is displayed for the sake of clarity) act as lattice-symmetry-breaking points at which extra [001]-elongated arms nucleate heterogeneously and grow crystallographically mismatched with the pre-existing anatase TiO_2 lattice substrate (cf. Figure 6c,d).

the *a*-axis and *b*-axis as well as along the equivalent transversal [101] and [011]. These expectations are indeed consistent with the particular architectural pattern of the sheaf-/bundle-like *I*-BNCs, which has been deciphered by means of HRTEM investigations (Figure 5). This is sketched in Scheme 2. The HRTEM projections are interpretable in terms of condensation of irregularly stretched, truncated octahedral bipyramidal units (which hence appear as hexagons in <1,0,0> projections) that are individually enclosed by a majority of (011)/(101)-type facets on the longitudinal walls and terminated by (001)-type facets at the opposite basal sides. Building blocks of this type recall equilibrium-growth shapes predicted for unpassivated TiO_2 anatase crystals on the basis of the Wulff construction.[26] The main nanorod branches of the *I*-BNCs therefore correspond to chains of such bipyramidal units aligned in the *c*-axis-direction.[26] Formally, branch regions are realized when such [001]-elongated arms bridge transversally along the [010]/[100] and/or [011]/[101] through one or more intervening bipyramidal blocks, leading to parallelization and/or bifurcation of some nanorod stems.[26,35] The monocrystalline nature of the *I*-BNCs, where the component arms are coherently crystallographically matched with each other (cf. Scheme 2 and Figure 5e−h), indicates that the *primary branching* event on homogeneously nucleated nanocrystal seeds can indeed be driven by the inherent anisotropy and centrosymmetry of the tetragonal lattice structure of the constituent anatase phase without intervention of crystal defects to break an otherwise all-linear growth symmetry.[25,50]

By comparison, the peculiar polycrystalline-like textured architecture of the *II*-BNCs (Figure 6) suggested that the latter should evolve from their parent monocrystalline *I*-BNCs through a different mechanism of growth-symmetry deviation. The multibundle/multifantail topologies of the *II*-BNCs resemble the hierarchical morphologies of recently reported nanocrystals of iron and cobalt phosphides, bismuth sulfide, and lanthanide orthovanadate, which have been assumed to result from a colloidal crystal-splitting mechanism mediated by multiple twin boundaries, analogous to that occurring in natural mineralization.[25] As to the present case, given the low probability of twin plane formation in TiO_2 anatase[24,51] it is plausible to assume that some of those Ti_5O_5 domains, which were found to decorate the surface of the *I*-BNCs, indeed acted as foreign *secondary heterogeneous branching* centers at which the tetragonal symmetry of the preformed anatase lattice underneath could be interrupted.[2−4,6,11,16,23,24] The proposed pathway is exemplified in Scheme 3. In a similar way, additional sources of growth anisotropy could be provided by surface sites with local defective structure (e.g., due to nonstoichiometry, local oxygen vacancy ordering), the occurrence of which is not uncommon in TiO_2.[26,52] Such sites could potentially serve as lattice-symmetry-breaking points. Thus, *II*-BNCs could result from two concomitant processes: (i) continued development of the pre-existing arms in the parent *I*-BNCs and (ii) generation of new monocrystalline, [001]-elongated branches that would depart from the foreign Ti_5O_5 domains and/or other defective locations, then growing crystallographically decoupled from their *I*-BNC skeleton substrates (cf. Scheme 3 and Figure 6c,d).

b. Thermodynamic Description. Taking into account the favorable structural prerequisites to branching and anisotropic development discussed above, the overall size and shape evolution of the BNCs can be understood by evaluating the change in the total free energy of growth, which accompanies the different stages of BNC formation. For a nanocrystal the total free energy of growth is determined by the balance between a surface-energy term (the energy that must be spent to create new solid/solution interfaces) and a volume term (the chemical potential earned when solution monomers are incorporated to the growing seeds).[2,53] The former contribution will particularly influence growth as long as the nanocrystals are appreciably small and/or expose unstable facets, while the latter will become increasingly important in more advanced evolution stages at larger particle sizes.

The high chemical potential environment built up by the aminolysis reaction during the incubation period triggers homogeneous nucleation of tiny anatase clusters, which are not only kinetically favored but also thermodynamically justified on the basis of the size dependence of the relative TiO_2 polymorph stability.[26] The just-nucleated atomic clusters will likely adopt shapes far diverging from the truncated bipyramidal habit predicted for equilibrium-grown bulk crystals.[26] However, as their growth advances, the embryos can be expected to accommodate a dominant fraction of lowest-energy (001)- and (101)/(011)-type facets. The latter actually represent the exclusive sets of surfaces that were ascertained to enclose our BNCs at all detectable growth stages (Figures 5 and 6).

The seeds can be assumed to sequentially approach some critical size/shape thresholds at which anisotropic radial splitting and subsequent concerted arm development, respectively, may in turn become thermodynamically favorable over both all-isotropic and all-linear growth. Progression toward such crossover points should be driven by independent alterations in the relevant free surface energy and volume terms that allow reaching selected minima in the total free energy of nanocrystal formation as the solution environment changes over time.[2,4a,49,53]

Now, in the early postnucleation stages, competitive OLAM and OLAC adsorption on seeds that have surpassed a limiting geometry can affect the relative stability order of the exposed facets to the point of making near-isotropic crystal development along the selected [001], [011]/[101], and [010]/[100] directions provisionally preferred.[35] Induction of *primary branching* can thus be regarded as a process that allows minimization of the solubility of the critical-size seeds by adjusting the overall (001) to (101)/(011)-type facet composition as a means to reduce their total surface free energy. This picture explains why the degree of ramification in *I*-BNCs was correlated with the surfactant composition of the initial reaction mixture. In this regard, it can be further considered that, since relatively higher temperatures weaken the surface binding strength and coverage density of surfactants, harsher synthesis conditions are likely to smooth out the surface energies of all relevant facets, thus attenuating the ultimate degree of branching achievable.

Once the splitting seeds have rapidly grown and crossed the successive critical volume threshold, the splitting process terminates, and growth switches to a regime characterized by almost exclusive development of anisotropic [001]-extended branches. This evolution mode thus represents a more convenient pathway to TiO_2 surface energy minimization in a solution in which OLAM has almost been exhausted due to completion of the aminolysis reaction, and the monomers are increasingly being depleted due to advancement of TiO_2 growth, respectively. In the modified, OLAC-dominated environment, (011)/(101) facets are far more stable (less soluble) than the (001) ones, which stimulates formation of sheaf-like *I*-BNCs with [001]-elongated arms that can accommodate increasingly extended (011)/(101)-stepped longitudinal sidewalls while maintaining a constantly low (001) surface area at their apexes. This evolution is propelled by an appropriate balance of monomer utilization in the nucleation and growth stages, respectively, whereby a relatively higher availability of reactive species is guaranteed per each nucleated seed that has split out. Such condition provides the volume-term contribution required to sustain the significant size increases associated with branching and anisotropic nanocrystal development.[2,4,49]

The temporary detection of small Ti_5O_5 domains decorating the *I*-BNCs prior to their development into *II*-BNCs clearly highlights the structural metastability of this unexpected phase on the nanoscale under our synthesis conditions. The Ti_5O_5 clusters may soon tend to dissolve due to the exceedingly diluted monomer concentration or to convert to anatase as the size crossover for polymorph stability reversal[26] is surpassed.

In multi-injection syntheses to *II*-BNCs, the environment containing their precursor *I*-BNCs is slowly replenished with reactive species originating from Ti-OLAC pyrolysis. The intermittent OLAC and $TiCl_4$ injections at each addition step lead to a rather moderate supersaturation level that follows a time variation qualitatively similar to that underlying the previous *I*-BNC growth. The particular OLAC-enriched solution chemical environment guarantees fulfilment of selective conditions for induction of *secondary branching* on the pre-existing *I*-BNCs (e.g., via heterogeneous nucleation at Ti_5O_5 and/or at defective surface sites) and subsequent extra arm growth. The overall size and shape transition to *I*-BNCs to *II*-BNCs can then be explained on the basis of nucleation−growth and energy balance arguments analogous to those used above.

Finally, another aspect deserving remark is that under our synthesis conditions TiO_2 BNCs can entirely grow in the anatase phase up to significantly large volumes, at which transformation to the more thermodynamically stable brookite[47] and/or rutile[26] may instead be expected. Phase conversion should be especially facilitated as the BNCs evolve and/or are annealed at low monomer supersaturation, i.e., under conditions approaching near-equilibrium growth. To shed light on this issue, we additionally investigated single-step syntheses in which the initial OLAM:OLAC ratio in the reaction mixture was systematically increased, and accordingly, the contribution of the aminolysis reaction to TiO_2 formation became progressively more dominant over that of the pyrolysis pathways. These control syntheses allowed verifying the progressive crossing of different growth regimes, in which the hypersplit anatase *I*-BNCs, slightly branched (bifurcated and chromosome-like) anatase nanorods, anatase spheres, and brookite nanorods (discussed in detail elsewhere[47]) were, in turn, obtained with high yield, respectively (Figures S6 and S7 in the Supporting Information). These findings highlighted that the geometric features and the crystal phase adopted by TiO_2 nanocrystals were strictly correlated with each other in a way that depended on the particular surfactant and monomer environment in which the nanocrystals were generated. Thus, the result of growing BNCs by the present route demonstrates that the thermodynamic stability of anatase TiO_2 can effectively be preserved over a broad size range as long as the nanocrystals forming in this phase adopt anisotropic branched morphologies enclosed by the particular distribution of facets that are indeed preferred in OLAC-rich media.

c. Kinetic Growth Model. The extreme sharpness of the *primary* solid-to-split seed transition as well as of the *secondary branching* event, on one side, and the generally fast rate of arm development, on the other side, highlight that branching-out and anisotropic growth should both be kinetically controlled processes. We suggest that the current results can be further understood by assuming that the overall shape evolution takes place in a diffusion-limited growth regime, under conditions where spatially inhomogeneous monomer fluxes accentuate nanocrystal development along crystallographic directions corresponding to the most reactive surface lattice sites.[2,49] The proposed mechanism is sketched in Scheme 4 and discussed as follows.

The hypothesis of reaction-controlled growth, in which BNC formation would be solely governed by the intrinsic rate at which the monomers are incorporated into the crystals, conflicts with our experimental evidence. Establishment of such a regime would require a constant monomer concentration throughout the bulk solution as well as in proximity of the nanocrystals. As long as the solution chemical potential persists above the level corresponding to the lattice atoms, the addition rate of monomers at each facet should be proportional to their concentration and the actual surface area exposed. Apparently, in spite of the favorable anisotropy of the tetragonal lattice and its centrosymmetry, a reaction-controlled mechanism fails to explain why branching does not ultimately produce radial-split morphologies (e.g., spherulites), where arms depart equally in all space directions from a central core,[25,50] but can instead lead to sheaf-like or bundle-type shapes. In addition, it remains elusive as to why the

Scheme 4. Proposed Diffusion-Controlled Growth Mechanism for the Formation of BNCs[a]

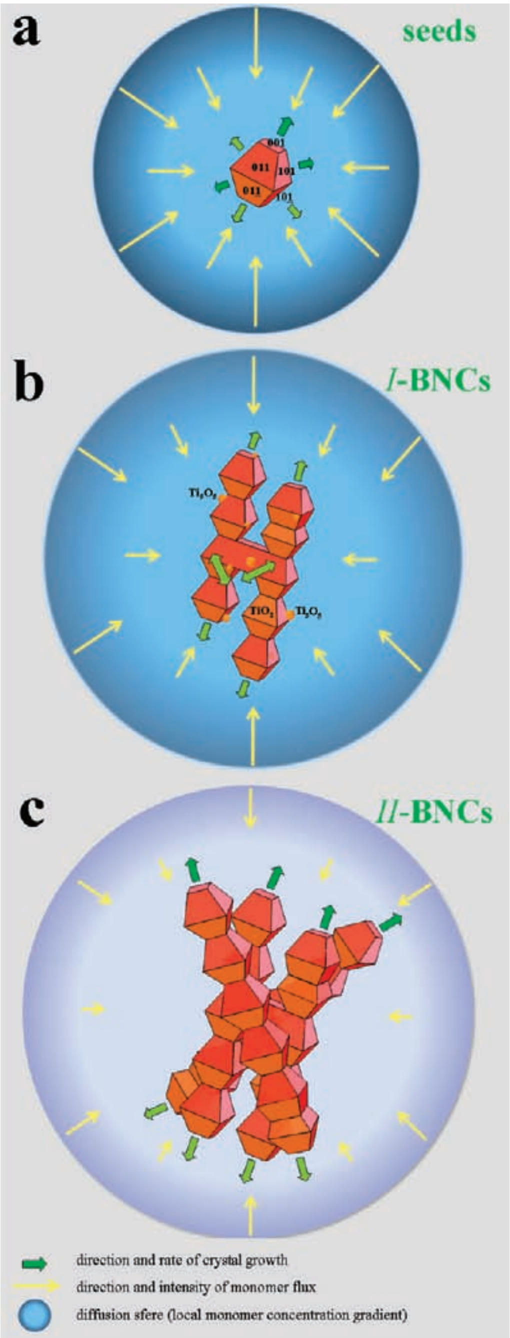

[a] The circle in each stage represents the interface boundary between the bulk solution and the diffusion sphere. The color shade of the circle reflects the distribution of monomer concentration gradient within the diffusion sphere. The direction and length of yellow arrows denote the direction and relative intensity of the monomer fluxes. The direction and length of green arrows denote the main crystallographic directions and relative rate of TiO_2 lattice growth.

BNC arms develop anisotropically while maintaining a nearly constant short axis, almost regardless of the actual monomer concentration and its time variation along the course of the respective synthesis stages.

More realistically, supersaturation levels high enough to guarantee reaction-controlled conditions may hold around the seeds only in a short period subsequent to nucleation, after which the system should enter a diffusion-controlled regime where growth is eventually restricted by the rate of long-distance reactant transport.[2,4] Each seed should be immersed within a stagnant liquid volume (i.e., the diffusion layer) along which the slow monomer flux directed from the bulk solution/diffusion−sphere interface to the seed surface generates an inward-decreasing concentration gradient[2,4] (Scheme 4a). The steepness of the gradient will depend on the relative amount of monomers left after the nucleation, which will be inversely proportional to initial supersaturation degree dictated by the aminolysis reaction (see previous paragraphs). According to the Mullins−Seserka instability model,[2,50,53] violent growth fluctuations within the solution layer most adjacent to the starting seeds can locally accelerate monomer addition to the highest-energy and/or more chemically reactive surface sites (e.g., edges, corners, or unstable facets exposed), which would thus tend to evolve preferentially along the corresponding crystallographic directions. The seeds can be thus driven to split out along the fastest-growing [001], [011]/[101], and [010]/[100] directions at different rates, determined by their respective reactivity and OLAM/OLAC adsorption thereon. Over time, the diffusion layer extends in space, and the gradient is smoothed out, leading to significant monomer depletion close to the innermost nanocrystal surface regions and, consequently, to decrease of the frequency with which the split core seed and thereof emerged arms further branch out. This paves the way to anisotropic evolution of *I*-BNCs with sheaf- or bundle-like architectures, depending on the balance of splitting events and competing growth along the relevant branch directions (Scheme 4b). The gradient drop attenuates the reactivity of all facets exposed, however impacting on the unique (00 ± 1) ones the least, because of their still far higher chemical potential. Therefore, subsequent growth in the OLAC-enriching environment will proceed preferentially along the [001]. In these circumstances, the terminal sections of the emerging branches will increasingly protrude into zones of the diffusion layer where they can selectively experience a proportionally higher supersaturation. As a result, arms can exhibit an exceptionally rapid-advancing growth front along the main elongation direction and almost negligible thickening of their short axis. An additional contribution to anisotropic growth propulsion arises from delayed incorporation of monomers that may have been "trapped" within the recessed nanoscale spaces intervening among contiguous arms.[50] Overall, the above considered dynamics, compatible with an autocatalytic growth mode, could not only lead to accentuation of the propensity toward anisotropic evolution naturally offered by the anatase structure but also permit one-dimensional development of *I*-BNCs to be sustained even when the monomer concentration has been greatly exhausted (Scheme 4b).

The minority metastable Ti_5O_5 domains, which accompanied *I*-BNC formation, should mainly result from random heterogeneous nucleation events that become kinetically favored when diffusional fluctuations increase the local supersaturation at some high-energy surface sites (most probably defects, corners, edges) (Scheme 4b). As highlighted earlier, the structurally different split architecture of the *II*-BNCs indicates that the latter evolve from their parent *I*-BNCs through a different mechanism of crystallographically misoriented branching, in which the Ti_5O_5 clusters are likely to play a role as lattice-symmetry-breaking points (Scheme 3). In the framework of the current kinetic interpretation of BNC evolution, it can be additionally suggested that some Ti_5O_5 sites with critical size and faceting, which survive dissolution, can serve as foreign catalyst centers at which heterogeneous nucleation of anatase TiO_2 may require overcoming a significantly lower activation energy barrier than that hindering growth continuation of the premade *I*-BNC body.[2,47] Thus, as the bulk solution becomes enriched with the pyrolysis-derived monomers during secondary reactant injections, the renewed, albeit mild, fresh flux of incoming monomers would selectively impact such reactive Ti_5O_5 centers compared to other locations on the *I*-BNC surface. Propelled by the peculiar reactivity of the available monomers, new anisotropic anatase domains (i.e., secondary branches) could rapidly emerge via seed-catalyzed or solution-liquid−solid growth pathways,[2,21] accompanied by destabilization of the Ti_5O_5 seed phase underneath and its polytypic conversion to anatase. Because of their exceedingly fast development rate, the newly implanted branches can rapidly approach the dimensions of the pre-existent arms, soon entering the diffusion-limited growth condition under which anisotropic development can be further sustained, as described above (Scheme 4c). This is consistent with the observation of *II*-BNCs with equally long arms at all synthesis stages.

Finally, it is worth stressing that, within the frame of the kinetically controlled growth mechanism proposed above, an important role in the stabilization of anatase BNCs in all growth stages should be played by the dynamic adhesion of surface-binding OLAC ligands. The latter could contribute to the trapping of the anatase structure by kinetically freezing the particular sets of facets exposed through both electronic and steric effects.[2,4a,47,54,55] This could provide a supplementary argument explaining the retention of the anatase structure up to very large sizes.

3.4. Application in Dye-Sensitized Solar Cells. The BNCs have been exploited as building blocks in DSSCs based on a standard FTO/TiO_2/Pt-FTO sandwiched configuration with the N719 dye as a TiO_2 sensitizer and I^-/I_3^- redox couple electrolyte (note that neither a scattering layer was introduced nor a $TiCl_4$ treatment was applied).[27,28,39] To this purpose, we have engineered high-quality BNC-based thin-film photoelectrodes that possess an underlying mesoporous structure suitable to maximize dye adsorption for light harvesting and nanocrystal interconnectivity for efficient electron diffusion. Our fabrication process guarantees substantial preservation of the native crystal phase and geometric features of the precursor BNCs utilized, thereby allowing genuine assessment of the correlation between photoanode structure and photovoltaic performances. As demonstrative examples, in the following paragraphs we report on DSSCs fabricated using sheaf-like *I*-BNCs and compact bundle-to-thread-shaped *II*-BNCs with projected short-/long-axis dimensions of 10−15 nm × 60−70 nm and 20−25 nm × 110−120 nm, respectively (Figure S8 in the Supporting Information), and compare them with corresponding benchmark cells based on commercial TiO_2 P25 Degussa (made of polydisperse, irregularly faceted nanocrystals of 20−50 nm, with anatase:rutile weight percentage of 20:80, Figure S9 in the Supporting Information).

3.4.1. Photoelectrode Fabrication. A key step in the processing of BNCs into high-quality thin-film photoelectrodes involved the development of suitable screen-printable TiO_2-based pastes.[30d−f,39] Our preparation strategy relied on directly combining the as-synthesized surfactant-capped BNCs with appropriate additives, namely, ethyl cellulose and α-terpineol, by means of a nonpolar volatile dispersing medium (toluene) in which all components were fully soluble at a mild temperature (60 °C). The BNC-based pastes obtained after solvent removal were easily manipulated and deposited onto an FTO substrate by the doctor-blade technique and finally subjected to programmed sequence of heating steps (up to 480 °C) in air to burn the organics off and induce crystal sintering.[27,29c,30f,30g,39] This procedure ultimately allowed reproducible fabrication of BNC-based thin films with tunable thickness (3−10 μm), which exhibited excellent adhesion and mechanical stability as well as good optical transparency (relative to the FTO glass substrate) in the visible range (Figure S10 in the Supporting Information). Figure 7 demonstrates the structural-morphological features of the photoelectrodes. The sintered films showed regular thickness and homogeneous texture without any detectable micrometer-size aggregates and cracks over areas of several squared micrometers. SEM inspection at variable magnifications (Figure 7a,b, d,e) revealed formation of a continuous spongy network of individually distinguishable nanoscale building blocks, which were interconnected through small junction points at random locations and appeared to be frequently accommodated with their longitudinal axis lying roughly parallel to the substrate underneath. Interestingly, such identified units possessed dimensional and morphological features closely resembling those of the starting BNCs (Figure S8 in the Supporting Information). Indeed, the characteristic rod-shaped details of arm shape anisotropy and body branching-out in *I*-BNCs made of fanned sheaf-like skeletons as well as in compact bundle-like *II*-BNCs with variable braid- and single-/double-ponytail profiles were indeed recognizable across individual building blocks of corresponding films (Figure 7b,e), with a level of detail comparable to that offered by low-resolution TEM imaging (cf. Figure S8 in the Supporting Information). This is the first time that unambiguous retention of the size-morphological features of branched colloidal nanostructures has been demonstrated for sintered photoelectrodes thereof.[17,18]

XRD analyses confirmed that the annealed films had fully retained the pristine anatase structure (Figure 7c,f). Calculation of the refined lattice parameters[40] evidenced that the lattice strain found in the as-prepared BNCs had been relieved to a noticeable extent. Actually, the average degree of expansion of the anatase unit cell volume, relative to the bulk material, had been leveled off down to 1.91% due to little residual dilatation of the *c*-axis ($a = b = 0.379$ nm, $c = 0.964$ nm in both cases). In addition, the thermal treatment had caused remarkable shrinking of all reflections (many of which indeed approached the IRF width) along with a significant abatement of the (004) peak intensity (cf. Figure 4), which transcribed into remarkably altered spectral signature of the shape anisotropy otherwise evidenced for the starting BNCs. From XRD data fitting,[40] the mean domain sizes, $D_{[004]}$, $D_{[200]/[020]}$, and $D_{[101]/[011]}$, were estimated to be >40, ∼31, and ∼18 nm for the *I*-BNC-derived films and >40 nm in all cases for the *II*-BNC-derived films, respectively. These values clearly exceeded the geometric features of individual BNC units in the sintered films, as measured by SEM. Such discrepancy between XRD and SEM observations can be explained as arising from the concurrence of various effects, including slight domain growth, associated, for example, with partial filling of the original branched structure at some of the recessed regions of the split body, increased degree of crystallinity, and overall reduced lattice strain following annealing of lattice defects and surface restructuring (after removal of the surfactant capping). In addition, it

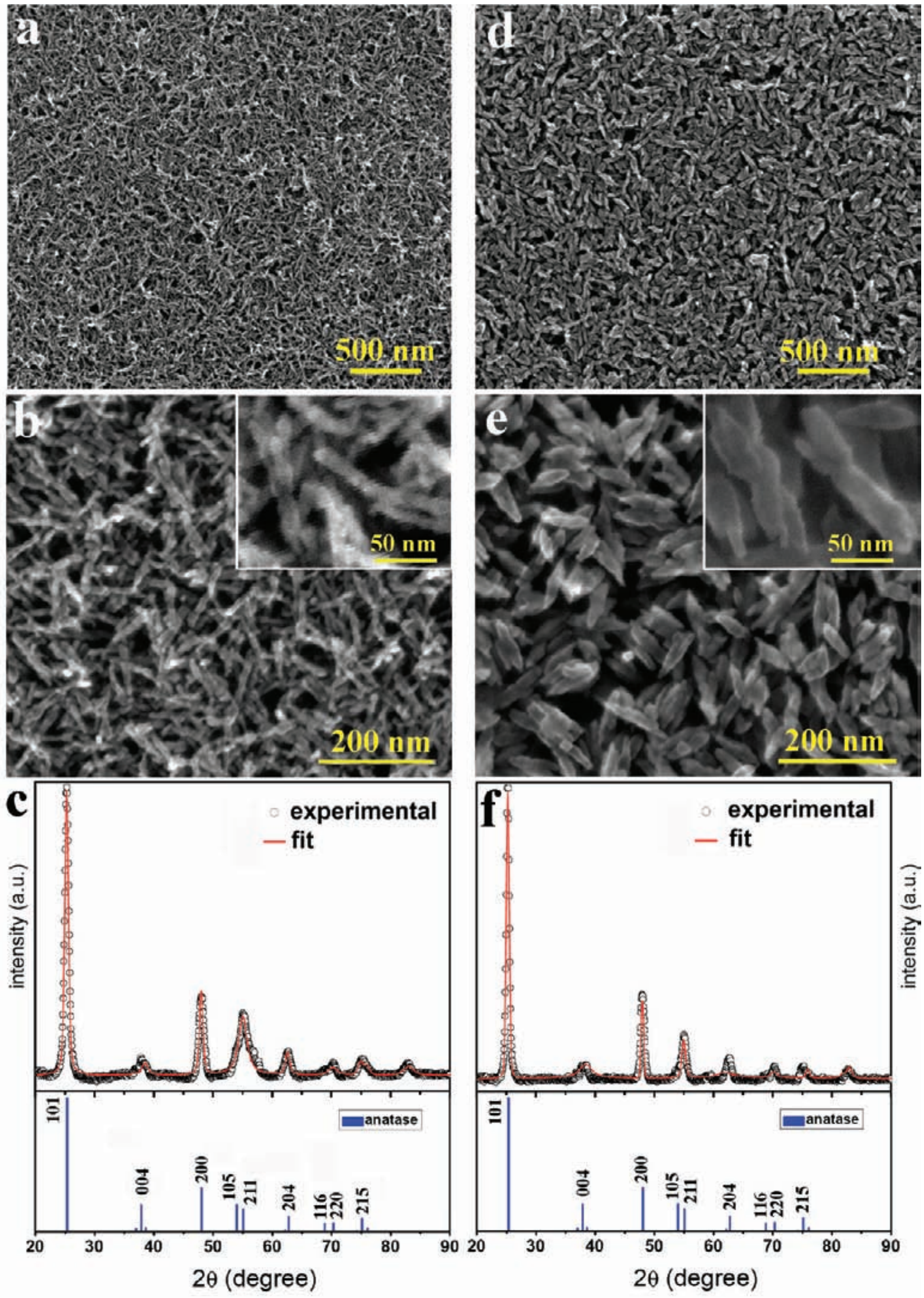

Figure 7. Structural and morphological characterization of sintered TiO_2 thin-film photoelectrodes fabricated starting from 10−15 nm × 60−70 nm *I*-BNCs (a−c) and 20−25 nm × 110−120 nm *II*-BNCs (d−f), respectively. The panels show: SEM overviews at variable magnifications (a,b, d,e) and experimental XRD patterns (dotted lines) along with the corresponding Rietveld-based fits (continuous lines) (c, f). The GOF indicators were <3 in both cases.

should be considered that the hypothesis of randomicity of the scattering domains, which normally applies to nanocrystal powder samples, no longer holds valid in the case of thin films, where preferred grain orientations and/or mosaicity (which are not accountable by the fitting procedure) can in fact alter the relative peak widths and intensities, thereby leading to overestimation of the crystalline domain sizes.[56]

The dye-loading capabilities of the photoelectrodes were assessed by spectrophotometric determination of the corresponding amounts of dye molecules desorbed in an alkaline medium (Figure S10 in the Supporting Information). As an example, 5 μm thick films assembled from *I*-BNCs and *II*-BNCs were found to accommodate a number of N719 molecules per projected device unit area as high as 1.50×10^{-7} and 1.02×10^{-7} mol/cm^2, respectively, which was appreciably larger than the dye amount loaded on the corresponding photoanodes made from TiO_2 P25 Degussa (0.60×10^{-7} mol/cm^2). This result indicated that the BNC units offered significant availability of sites for N719 anchoring, in spite of their noticeable bulkiness relative to the P25 Degussa counterparts and of the possible surface area losses caused by elimination of the crystal split structure at some recessed locations of the BNC skeletons. The superior dye-adsorption properties of the BNC-based photoelectrodes should correlate with the particular anisotropic ramified topology and surface distribution of the underlying building blocks. Indeed, it is useful to recall that the BNCs possessed [001]-elongated arms with longitudinal sidewalls almost exclusively exposing families of equivalent (101)/(011)-type facets. The latter may indeed be supposed to be inherently more prone to coordinate to the carboxylate moieties of N719 molecules, relative to other anatase surfaces.[57]

Taken together, the results reported above suggest that the desirable quality features embodied by our BNC photoelectrodes should primarily be associated with the particular properties of the newly developed screen-printable TiO_2-based pastes utilized as film precursors. Conventional paste preparation protocols generally involve several delicate steps in which dry (uncapped) nanoparticles are mixed with several additives and dispersing solvents (the latter are normally unable to solvate all other ingredients) and subjected to controlled stirring, grinding, and/or ultrasound irradiation.[17,18,27,28,39] Such procedures aim at disrupting nanoparticle aggregates and ensure spatially homogeneous sintering conditions during the subsequent thermal annealing, however often at the cost of irreproducible photoelectrode features. In contrast, profiting from the unique property of complete miscibility of our hydrophobic surfactant-capped BNCs, ethyl cellulose and α-terpineol in a common medium (toluene), we could easily prepare extremely homogeneous pastes by combining an optically transparent toluene solution of BNCs with the two additives. The uniformly dispersed state of the three components allowed ethyl cellulose and α-terpineol to serve as effective protective-binding and solvating agents, respectively,[27,28,30d−30f,39] for the BNCs. These functions can be understood as follows.

In the first mixing step, the hydrophobic oleate surfactant shell on the TiO_2 BNCs, which originally engulfs only solvent molecules, tends to enwrap ethyl cellulose molecules that may additionally coordinate to vacant TiO_2 surface sites via their free −OH moieties, eventually attributing an overall increased compactness and steric hindrance to the nanocrystal capping layer. Concomitant to this, the outermost exposed −OH groups of intercalated ethyl cellulose molecules can drive the BNCs to closely interact and group into free-standing, loosely bound aggregates, thus yielding a homogeneous and opalescent solution. In the second preparation step, exchange of the toluene solvent for α-terpineol leads to highly viscous and stable pastes where free-standing BNCs and reversible assemblies thereof are uniformly dispersed within a high-boiling liquid matrix. Upon suitably programmed heating of the pastes spread over FTO, the organic components can be burnt off slowly enough to allow the BNCs to delicately interconnect and form networked films that sintered to the glass substrate without collapsing into macroscopic segregated agglomerates and/or generating extensive cracks. In this regard, the observed retention of the anatase structure as well as of the size/shape features of the original BNCs can be understood as resulting from two main synergistically operating mechanisms. First, the oleate anions tightly bound to the starting BNCs can efficiently stabilize high-energy surface sites (e.g., edges, corners, and defects) at which crystal phase conversions and/or lattice fusion pathways are likely to initiate due to the higher mobility of atoms exposed thereon.[26,58,52] Second, the bulky ethyl cellulose molecules enwrapped within the surfactant shell and the ubiquitous α-terpineol liquid matrix can jointly act as further moderators of the solid-state reactivity of the BNCs, inhibiting their premature, irreversible coalescence, while allowing their crystallinity degree to increase during the thermal treatment (e.g., upon annealing of lattice defects). These arguments explain why our photoelectrode fabrication approach guaranteed preservation of the BNCs from detrimental phase transformations and/or dramatic size/shape modifications which are instead normally induced in dry powders of nanocrystallite aggregates or uncapped TiO_2 nanoparticles when the latter are subjected to harsh heating conditions (at >400 °C).[17,18,28]

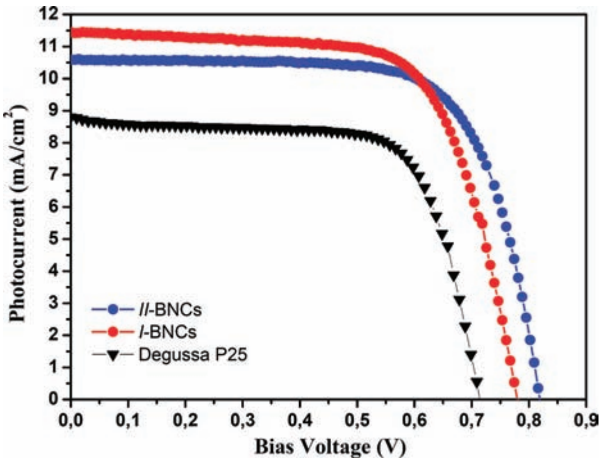

Figure 8. $I-V$ curves recorded for 10 μm thick photoelectrodes based on 10−15 nm × 60−70 nm *I*-BNCs, 20−25 nm × 110−120 nm *II*-BNCs (cf. Figure 7), and commercial TiO_2 Degussa P25 nanoparticles, respectively.

3.4.2. Device Performance Assessment. The performances of BNC-based DSSCs were comparatively examined under standard illumination test conditions (AM1.5G) with respect to those achieved with benchmark devices based on commercial TiO_2 P25 Degussa. Figure 8 displays the relevant photocurrent−voltage ($I-V$) curves. As indicated by the energy conversion efficiency (η), fill factor (FF), open circuit voltage (V_{OC}), and short-circuit current density (J_{SC}) values listed in Table 1, the BNC-based devices exhibited appreciable performances relative to the P25-based reference for photoelectrode thicknesses spanning the 3−10 μm interval. The significance of the measured parameters is discussed in detail in the next paragraphs.

The photocurrent intensity, J_{SC}, ranged from 3.9 to 11.43 mA/cm^2 for gradually thicker TiO_2 films, reflecting the extent of dye loading attained in the respective cases. It was notable that the DSSCs fabricated with the bulkier *II*-BNCs exhibited fairly pronounced J_{SC} relative to their *I*-BNC-based counterparts (10.52 vs 11.43 mA/cm^2 for 10 μm thickness) in spite of the proportionally much lower (by ∼50%) amount of adsorbed N719. This fact preliminarily indicated that the relatively lower photon-harvesting capability of the *II*-BNC-based cells, which was ultimately dictated by their active surface area, was satisfactorily offset by more efficient charge collection and transport properties enabled by the existence of spatially extended crystal domains available for fast electron diffusion[28] (see EIS data below). In addition, all BNC-built DSSCs exhibited the highest V_{OC} values, which ranged from ∼0.78 to ∼0.84 V, whereas

Table 1. Photovoltaic Performances of DSSCs Based on Variable-Thickness Photoelectrodes Fabricated from BNCs and TiO_2 P25 Degussa Nanoparticles, Respectively

	I-BNCs (10−15 nm × 70−80 nm)				*II*-BNCs (20−25 nm × 120−130 nm)				Degussa P25			
photoanode thickness [μm]	η [%]	V_{OC} [V]	J_{SC} [mA/cm^2]	FF	η [%]	V_{OC} [V]	J_{SC} [mA/cm^2]	FF	η [%]	V_{OC} [V]	J_{SC} [mA/cm^2]	FF
3.0	**2.7**	0.81	4.70	0.71	**2.5**	0.84	4.20	0.72	**2.0**	0.75	3.90	0.69
6.0	**4.4**	0.79	8.00	0.70	**4.2**	0.82	7.22	0.71	**2.9**	0.73	5.90	0.68
10.0	**6.2**	0.78	11.43	0.70	**6.0**	0.82	10.52	0.70	**4.4**	0.71	8.78	0.70

$V_{OC} < 0.75$ V was measured for the P25 cells. On the basis of the well-known diode equation analysis,[59] the increase in V_{OC} suggested that the overall kinetic balance of electron photogeneration and losses was remarkably favorable in BNC-made films. Such a property should arise from the comparatively lower density of defective contact boundaries holding among interlaced BNC units as well as good electron-transport properties enabled by the particular crystal directionality of the nanorod arm subcomponents and the pre-existing branch-type connectivity in individual BNCs.[28] The general tendency of J_{SC} to scale up linearly for gradually thicker TiO_2 films correlated with the corresponding V_{OC} variation. The slight V_{OC} decrease was caused by the opposing effect of the charge-recombination centers that in fact accumulated as the overall TiO_2 surface area expanded with increasing film thickness.[26,27,60] Ultimately, DSSCs fabricated from our BNCs reached η as high as 6.2% for 10 μm thick photoelectrodes, which was ~30% above the efficiency achievable with the reference P25-based cells. These performances, which rank among the best so far reported for DSSCs based on colloidal anisotropic nanocrystals (using the same device configuration), largely overcome the highest ever achieved by DSSCs based on both wet-chemically prepared and substrate-grown branched nanostructures.[17,18,28,29f−29h] Actually, a comparison between the present results and the photovoltaic responses of recently developed DSSCs built starting from colloidal rutile-phase TiO_2 star-like BNCs made of 25 nm × 450 nm arms (η = 2.1%)[18] or 20−40 nm × 150 nm saw-like nanostructures (η = 4.3%),[17] highlights the advantageous roles played by the particular micro-/nanostructural features of our photoelectrodes on their ultimate energy conversion efficiency. Major benefits can indeed be expected to result from attainment of a percolation network entirely made of the most favorable anatase phase, where the interconnected BNC units comprise prejoint arm subcomponents with thin diameter and high aspect ratio with surface composition amenable to extensive dye adsorption. The measured photovoltaic parameters accordingly suggested achievement of a satisfactory combination of light-harvesting capabilities and efficient transfer of the photoinjected electrons to the collecting electrode.

To scrutinize the inherent electron-transport properties of the BNC-based devices, we performed EIS measurements[61−66] at an applied voltage of 0.8 V (close to V_{OC}) in the dark at frequencies lying in the 30 mHz −100 kHz range. As a representative case of study, Figure 9 displays the EIS spectra recorded for 10 μm thick photoelectrodes. The arcs observable in the Nyquist diagram reveal the existence of defined electrochemical interfaces with different time constants.[61,62,65,66] The highest-frequency arc (>1000 Hz, corresponding to the leftmost portion of the diagram) is due to the parallel coupling of the capacitances of the FTO-Pt/electrolyte and the FTO/electrolyte interfaces and the sum of the resistances at the FTO/TiO_2 and FTO-Pt/electrolyte interfaces. This arc is nearly independent of the bias voltage.[63] The largest medium-frequency (1000−10 Hz) arc is related to electron transport across the mesoporous TiO_2 films, which competes with electron losses mainly due to I_3^- reduction and back reactions at the dye-sensitized TiO_2/electrolyte interface. A minor lowest-frequency (<10 Hz) arc may be additionally detected (in the rightmost region of the diagram), which correlates with the diffusion of I_3^- ions (holes) through the electrolyte.[61,62,65]

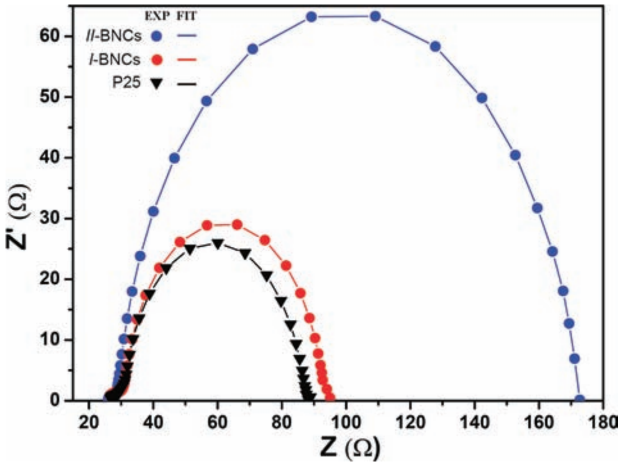

Figure 9. Experimental EIS spectra recorded in the dark at an applied voltage of 0.8 V for DSSCs based on 10−15 nm × 60−70 nm *I*-BNCs, 20−25 nm × 110−120 nm *II*-BNCs, and commercial TiO_2 Degussa P25 nanoparticles, respectively (cf. Figures 7 and 8). The corresponding fits (continuous lines) are also shown.

The EIS data were fitted on the basis of the established equivalent-circuit model by Wang et al.,[62,65] whereby constant-phase elements, instead of pure capacitors, are used to account for the uneven and porous structure of the photoelectrodes. Table 2 reports the values extrapolated for the following parameters: (i) the charge-transfer resistances at the FTO/TiO_2 and FTO-Pt/electrolyte interfaces, respectively, R_{CO} and R_{CE} (R_{CE} is generally much smaller than R_{CO} and varies only slightly as a function of the applied bias potential); (ii) the series double-layer capacitances, $C_{CO}//C_{CE}$, of the FTO/electrolyte and FTO-Pt/electrolyte interfaces, respectively, and the corresponding capacitor ideality coefficient, $a_{CO//CE}$; (iii) the electron-transport resistance of the TiO_2 photoelectrode, R_T, which depends on its mesoporous film structure; (iv) the charge-transfer resistance, R_{CT}, and the chemical capacitance, C_μ, at the dye-sensitized TiO_2/electrolyte interface; and (v) the electron diffusion length, L_e, that is, the average distance electrons can travel within the semiconductor (before recombining or being trapped), and their corresponding average lifetime, τ_e.

Table 2. Electrochemical Parameters of DSSCs Based on 10 μm Thick Photoelectrodes, Extracted by Fitting EIS Spectra (Figure 9) According to the Approach by Wang et al.[62]

photoanode material	R_{CO} + R_{CE} [Ω]	$C_{CO}//C_{CE}$ [μF]	$a_{CO//CE}$	$C_{\square}$ [μF]	R_{CT} [Ω]	R_T [Ω]	L_e [μm]	τ_e [ms]
commercial TiO_2 P25	8.9	1133.5	0.73	399.3	56.1	9.5	24.3	22.4
I-BNCs (10−15 nm × 70−80 nm)	4.7	874.2	0.96	280.7	62.7	15.7	19.9	17.6
II-BNCs (20−25 nm × 120−130 nm)	3.3	611.3	0.97	378.8	142.0	9.6	38.5	53.8

From the fitting of the highest-frequency EIS arc, it emerged that the BNC-built DSSCs were distinguished by an overall reduced charge-transfer resistance and remarkably less pronounced capacitive behavior at the relevant FTO/TiO_2 contact boundaries. Indeed, the deduced R_{CO} + R_{CE} and $C_{CO}//C_{CE}$ values were remarkably smaller than those associated with the P25-based device counterpart, respectively. These results indicated that the BNC films had attained improved electrical contact to their respective FTO substrates underneath (hence, the lower R_{CO}), which concurred to ultimately minimize charge accumulation at the FTO/TiO_2 interface.[67]

The analysis of the medium-frequency EIS arcs disclosed a generally enhanced charge-transfer resistance at TiO_2/electrolyte interfaces in the BNC-built DSSCs, relative to their P25 reference counterpart. In particular, the noticeably broad arc width associated with the *II*-BNC-based device, where the constituent building blocks possessed larger volumes, should mainly arise from a substantially lower occurrence of charge-trapping sites within the TiO_2 film, at which undesired reduction of I_3^- could be promoted by long-resident photoexcited electrons (R_{CT} = 142.0 Ω vs 56.1 Ω for P25). The correspondingly low R_T (9.6 Ω) as well as the superior V_{OC} (see Table 1) measured for these devices corroborated this interpretation. On the other hand, concerning the *I*-BNC-made DSSCs, the smaller EIS arc width could be correlated with a modest hindrance against electron losses in charge-recombination pathways (R_{CT} = 62.7 Ω) and the still appreciably large R_T of the photoelectrode (15.7 Ω). It is thus plausible that in this case major electron losses were caused by the existence of relatively higher density of crystal defects or other catalytic sites, especially at the surface (for example, in proximity of residual Ti_5O_5 domains) and at imperfect heterojunctions among neighboring *I*-BNCs, which could in fact act as charge trapping and/or recombination centers, thereby hindering electron diffusion across the mesoporous TiO_2 film.

At this point, it deserves recalling that the absolute values R_T and R_{CT} are of limited usefulness to the purpose of ranking the performances of different devices. For example, R_T and R_{CT} are both extensive parameters that scale with the overall TiO_2 surface area available and additionally depend on the actual number of grain boundaries and lattice defects in the films. As opposed, the R_{CT}/R_T ratio (see eq 2) is a more reliable indicator of the genuine electron-collection efficiency of the devices.[61] Therefore, to evaluate the inherent electron-transport properties of BNC-based cells, the EIS-derived fit parameters were used to estimate τ_e and L_e by means of the following equations based on the quasi-static approximation model developed by Bisquert et al.[66,68]

$$\tau_e = (C_\mu R_{CT}) \tag{1}$$

$$L_e = d(R_{CT}/R_T)^{1/2} \tag{2}$$

where d is the photoelectrode thickness. The calculations yielded τ_e = 17.6 ms and L_e =19.9 μm and τ_e = 53.8 ms and L_e = 38.5 μm for DSSCs based on *I*-BNCs and *II*-BNCs, respectively, while τ_e =22.4 ms and L_e = 24.3 μm were deduced for the reference P25-based cell (Table 2).

The significantly larger L_e and longer τ_e achieved in the *II*-BNC-made DSSCs suggested that BNC-based cells could indeed perform better than the Degussa P25 reference device in terms of electron-collection efficiencies, depending on the size-morphological features of the underlying TiO_2 building blocks. The networking of *II*-BNC units, which possessed longer crystallographically fused rod-shaped branches with defined lattice elongation direction prior to the sintering step, transcribed into more extended pathways amenable to fast electron percolation, on one side, and reduced occurrence of deleterious charge-trapping sites located at the surface and/or junction regions among interconnected nanocrystals, on the other side.[69,70] Consistent with the corresponding R_{CT} trends, the impact of charge recombination also appeared to be overall more attenuated in photoelectrodes that incorporated bulkier BNCs (cf. τ_e and L_e for *I*-BNCs vs *II*-BNCs). Hence, it can be safely deduced that anisotropic building blocks, which combine increasingly high aspect-ratio arm subcomponents arranged in expanded hypersplit topologies, can facilitate photoinjected electron diffusion across the film network, affording improved charge-collection properties that can largely overwhelm the deleterious effects of trapping/recombination events and compensate for even modest light-harvesting capabilities.

4. CONCLUSIONS

We have developed a nonaqueous sol−gel approach that opens access to a colloidal crystal-spitting growth regime, in which unique breeds of organic-capped TiO_2 BNCs, distinguished by anisotropic profile and tunable hyperbranched topologies, can be selectively generated in the metastable anatase phase over a broad size range (40−200 nm). Our synthetic strategy relies on a straightforward reactant supply technique that achieves sequential exploitation of aminolysis and pyrolysis of titanium oleate complexes in binary surfactant mixtures at 240−320 °C. Structural investigations have disclosed the peculiar branching patterns that underlie the new TiO_2 architectures. First-generation BNCs initially formed upon the aminolysis reaction possess a strained monocrystalline skeleton, while their corresponding second-generation derivatives fed by pyrolysis pathways accommodate additional arms crystallographically mismatched with the lattice underneath. The complex evolution of the new nanocrystal architectures has been thoroughly discussed on the basis of complementary mechanistic arguments. Thermodynamic pathways, associated with the inherent shape-directing effect of the chain-like anatase structure and free-energy changes accompanying branching and anisotropic development, have been proposed to interplay with kinetic processes, including spatially inhomogeneous, diffusion-limited monomer fluxes, lattice-symmetry breaking at transient Ti_5O_5 domains, and surfactant-induced stabilization. While enriching current knowledge of nanoscale TiO_2 crystallization in nonaqueous colloidal media, this study can be of both fundamental significance and practical usefulness for the development of generic and versatile synthetic tools to tailor nanocrystals with sophisticated shapes.

As a demonstration of the functionality of the newly developed branched nanoarchitectures, we have successfully processed BNCs with substantially unaltered size, morphology, and crystal structure into high-quality thin-film photoelectrodes for DSSCs. An energy conversion efficiency of 6.2% has been reached already with standard cells (based on 10 μm thick photoelectrodes), which overcomes the highest so far reported for previously developed split TiO_2 nanostructures synthesized by other routes. Analysis of the photovoltaic parameters suggested that the BNCs indeed allow light-harvesting and charge-collection properties that can significantly offset detrimental electron losses due to recombination and/or trapping events. Further improvements are therefore expected upon implementing BNCs with suitably engineered geometric features into DSSCs that are allowed to operate through increasingly sophisticated device configurations.

It is conceivable that the availability of these new hyperbranched architectures will also stimulate progress in all numerous fields that greatly benefit from colloidal crystal-phase and shape-controlled TiO_2 nanomaterials, such as optoelectronics, sensing, (photo)catalysis (e.g., for ambient detoxification, synthesis of organic, and fuel molecules), as well as energy production and storage (e.g., fuel cells, lithium-ion batteries), raising each of them to a new level of performance.

■ ASSOCIATED CONTENT

Ⓢ Supporting Information. Additional TEM and HRTEM images of as-synthesized nanocrystals; Dynamical multibeam calculation of numerical diffraction patterns of anatase TiO_2; Reference XRD pattern of bulk Ti_5O_5; FT-IR spectra of purified TiO_2 nanocrystals; Shape- and crystal-phase evolution of TiO_2 nanocrystals grown in OLAC:OLAM mixtures with variable composition; TEM and SEM images of the starting BNCs and commercial TiO_2 Degussa P25 nanoparticles used for DSSC fabrication; SEM images of thin-film photoelectrodes made from TiO_2 Degussa P25; UV−vis absorption spectra authenticating dye adsorption on the photoelectrodes. This material is available free of charge via the Internet at http://pubs.acs.org.

■ AUTHOR INFORMATION

Corresponding Author

davide.cozzoli@unisalento.it; davide.cozzoli@unile.it

Present Addresses

[#]The Molecular Foundry, Lawrence Berkeley National Laboratory, Berkeley, California 94720, United States.

■ ACKNOWLEDGMENT

Part of this work has been supported by the Italian Institute of Technology (IIT) Foundation through the project SEED XMI-LAB "X-ray synchrotron class rotating anode microsource for the structural micro imaging of nanomaterials and engineered biotissues" (IIT Protocol n. 21537). Benedetta Antonazzo is gratefully acknowledged for technical assistance with SEM measurements.

■ REFERENCES

(1) Ozin, G. A.; Arsenault, A. C.; Cademartiri, L. *Nanochemistry: A Chemical Approach to Nanomaterials*; RSC Publishing: Cambridge, 2008.

(2) *Advanced Wet-Chemical Synthetic Approaches to Inorganic Nanostructures*; Cozzoli, P.D., Ed.; Transworld Research Network: Kerala, India, 2008.

(3) Niederberger, M.; Pinna, N. *Metal Oxide Nanoparticles in Organic Solvents - Synthesis, Formation, Assembly and Application*; Springer: New York, 2009.

(4) (a) Jun, Y.-w.; Choi, J.-s.; Cheon, J. *Angew. Chem., Int. Ed.* **2006**, *45*, 3414–3439. (b) Viswanath, B.; Kundu, P.; Halder, A.; Ravishankar, N. *J. Phys. Chem. C* **2009**, *113*, 16866–16883.

(5) Carbone, L.; Cozzoli, P. D. *Nano Today* **2010**, *5*, 449–493.

(6) Lim, B.; Xia, Y. *Angew. Chem., Int. Ed.* **2011**, *50*, 76–85.

(7) Lim, B.; Jiang, M.; Camargo, P. H. C.; Cho, E. C.; Tao, J.; Lu, X.; Zhu, Y.; Xia, Y. *Science* **2009**, *324*, 1302–1305.

(8) Chen, Y.-H.; Hung, H.-H.; Huang, M. H. *J. Am. Chem. Soc.* **2009**, *131*, 9114–9121.

(9) Masuda, Y.; Ohji, T.; Kato, K. *Cryst. Growth Des.* **2009**, *10*, 913–922.

(10) Hu, W.; Li, L.; Li, G.; Tang, C.; Sun, L. *Cryst. Growth Des.* **2009**, *9*, 3676–3682.

(11) Krahne, R.; Manna, L. Tetrapod-shaped semiconductor nanocrystals. In *Handbook of Nanophysics: Nanoparticles and Quantum Dots*; Sattler, K., Ed.; CRC Press — Taylor and Francis: Boca Raton, Florida, United States, 2010.

(12) Jones, M. R.; Osberg, K. D.; Macfarlane, R. J.; Langille, M. R.; Mirkin, C. A. *Chem. Rev.* **2011**, *111*, 3736–3827.

(13) (a) Cozzoli, P. D.; Snoeck, E.; Garcia, M. A.; Giannini, C.; Guagliardi, A.; Cervellino, A.; Gozzo, F.; Hernando, A.; Achterhold, K.; Ciobanu, N.; Parak, F. G.; Cingolani, R.; Manna, L. *Nano Lett.* **2006**, *6*, 1966–1972. (b) Zitoun, D.; Pinna, N.; Frolet, N.; Belin, C. *J. Am. Chem. Soc.* **2005**, *127*, 15034–15035. (c) Zhang, H.-T.; Ding, J.; Chow, G.-M. *Langmuir* **2008**, *24*, 375–378. (d) He, S.; Garcia, I.; Gallo, J.; Penadés, S. *Cryst. Eng. Comm.* **2009**, *11*, 2605–2607. (e) Casavola, M.; Falqui, A.; Garcia, M. A.; Garcia-Hernandez, M.; Giannini, C.; Cingolani, R.; Cozzoli, P. D. *Nano Lett.* **2009**, *9*, 366–376.

(14) (a) Ould-Ely, T.; Prieto-Centurion, D.; Kumar, A.; Guo, W.; Knowles, W. V.; Asokan, S.; Wong, M. S.; Rusakova, I.; Luttge, A.; Whitmire, K. H. *Chem. Mater.* **2006**, *18*, 1821. (b) Hofmann, C.; Rusakova, I.; Ould-Ely, T.; Prieto-Centurión, D.; Hartman, K. B.; Kelly, A. T.; Lüttge, A.; Whitmire, K. H. *Adv. Funct. Mater.* **2008**, *18*, 1661–1667. (c) Han, X.-G.; Jin, M.-S.; Kuang, Q.; Zhou, X.; Xie, Z.-X.; Zheng, L.-S. *J. Phys. Chem. C* **2009**, *113*, 2867–2872.

(15) Liao, H.-G.; Jiang, Y.-X.; Zhou, Z.-Y.; Chen, S.-P.; Sun, S.-G. *Angew. Chem., Int. Ed.* **2008**, *47*, 9100–9103.

(16) Watt, J.; Cheong, S.; Toney, M. F.; Ingham, B.; Cookson, J.; Bishop, P. T.; Tilley, R. D. *ACS Nano* **2010**, *4*, 396–402.

(17) Oh, J.-K.; Lee, J.-K.; Kim, H.-S.; Han, S.-B.; Park, K.-W. *Chem. Mater.* **2010**, *22*, 1114–1118.

(18) Koo, B.; Park, J.; Kim, Y.; Choi, S.-H.; Sung, Y.-E.; Hyeon, T. *J. Phys. Chem. B* **2006**, *110*, 24318–24323.

(19) Luo, J.; Liu, C. M.; Yang, S. H.; Cao, Y. *Sol. Energy Mater. Sol. Cells* **2010**, *94*, 501–508.

(20) Corti, M; Lascialfari, A.; Micotti, E.; Castellano, A.; Donativi, M.; Quarta, A.; Cozzoli, P. D.; Manna, L.; Pellegrino, T.; Sangregorio, C. *J. Magn. Magn. Mater.* **2008**, *320*, e320–e323.

(21) Cozzoli, P. D.; Pellegrino, T.; Manna, L. *Chem. Soc. Rev.* **2006**, *35*, 1195–1208.

(22) Yong, K.-T.; Sahoo, Y.; Choudhury, K. R.; Swihart, M. T.; Minter, J. R.; Prasad, P. N. *Nano Lett.* **2006**, *6*, 709–714.

(23) He, M.; Yu, L.; Lu, X.; Feng, X. *J. Am. Ceram. Soc.* **2007**, *90*, 319–321.

(24) Jun, Y.-w.; Chung, H.-W.; Jang, J.-t.; Cheon, J. *J. Mater. Chem.* **2011**, *21*, 10283–10286.

(25) (a) Hu, Y. H.; Chen, K. Z. *J. Cryst. Growth* **2007**, *308*, 185–188. (b) Tang, J.; Alivisatos, A. P. *Nano Lett.* **2006**, *6*, 2701–2706. (c) Kelly, A. T.; Rusakova, I.; Ould-Ely, T.; Hofmann, C.; Luttge, A.; Whitmire, K. H.

Nano Lett. **2007**, *7*, 2920–2925. (d) He, J. H.; Han, M.; Shen, X. P.; Xu, Z. *J. Cryst. Growth* **2008**, *310*, 4581–4586. (e) Stavila, V.; Whitmire, K. H.; Rusakova, I. *Chem. Mater.* **2009**, *21*, 5456–5465. (f) Deng, H.; Liu, C.; Yang, S.; Xiao, S.; Zhou, Z.-K.; Wang, Q.-Q. *Cryst. Growth Des.* **2008**, *8*, 4432–4439. (g) Sun, Z. Z.; Feng, X. M.; Hou, W. H. *Nanotechnology* 2007, *18*, (45). (h) Pan, Q.; Huang, K.; Ni, S.; Yang, F.; Lin, S.; He, D. *J. Alloys Compd.* **2009**, *484*, 322–326. (i) Zhang, H.; Ha, D.-H.; Hovden, R.; Kourkoutis, L. F.; Robinson, R. D. *Nano Lett.* **2011**, *11*, 188–197.

(26) Chen, X.; Mao, S. S. *Chem. Rev.* **2007**, *107*, 2891–2959.

(27) Hagfeldt, A.; Boschloo, G.; Sun, L.; Kloo, L.; Pettersson, H. *Chem. Rev.* **2010**, *110*, 6595–6663.

(28) (a) Adachi, M.; Jiu, J.; Isoda, S. *Curr. Nanosci.* **2007**, *3*, 285–295. (b) Chun, J.; Lee, J. *Eur. J. Inorg. Chem.* **2010**, 4251–4263. (c) Zhang, Q.; Cao, G. *Nano Today* **2011**, *6*, 91–109.

(29) (a) Kang, S. H.; Choi, S.-H.; Kang, M.-S.; Kim, J.-Y.; Kim, H.-S.; Hyeon, T.; Sung, Y.-E. *Adv. Mater.* **2008**, *20*, 54–58. (b) Liu, B.; Aydil, E. S. *J. Am. Chem. Soc.* **2009**, *131*, 3985–3990. (c) Yang, W. G.; Wan, F. R.; Wang, Y. L.; Jiang, C. H. *Appl. Phys. Lett.* **2009**, *95*, 133121. (d) Lee, S.; Cho, I.-S.; Lee, J. H.; Kim, D. H.; Kim, D. W.; Kim, J. Y.; Shin, H.; Lee, J.-K.; Jung, H. S.; Park, N.-G.; Kim, K.; Ko, M. J.; Hong, K. S. *Chem. Mater.* **2010**, *22*, 1958–1965. (e) Enache-Pommer, E.; Liu, B.; Aydil, E. S. *Phys. Chem. Chem. Phys.* **2009**, *11*, 9648–9652. (f) Sauvage, F.; Di Fonzo, F.; Li Bassi, A.; Casari, C. S.; Russo, V.; Divitini, G.; Ducati, C.; Bottani, C. E.; Comte, P.; Grätzel, M. *Nano Lett.* **2010**, *10*, 2562–2567. (g) Wang, H.; Bai, Y.; Wu, Q.; Zhou, W.; Zhang, H.; Li, J.; Guo, L. *Phys. Chem. Chem. Phys.* **2011**, *13*, 7008–7013. (h) Liao, W.-P.; Wu, J.-J. *J. Mater. Chem.* **2011**, *21*, 9255–9262.

(30) (a) Yongcai, Q.; Wei, C.; Shihe, Y. *Angew. Chem. Int. Ed* **2010**, *49*, 3675–3679. (b) Saji, V. S.; Pyo, M. *Thin Solid Films* **2010**, *518*, 6542–6546. (c) Jiu, J.; Isoda, S.; Wang, F.; Adachi, M. *J. Phys. Chem. B* **2006**, *110*, 2087–2092. (d) De Marco, L.; Manca, M.; Giannuzzi, R.; Malara, F.; Melcarne, G.; Ciccarella, G.; Zama, I.; Cingolani, R.; Gigli, G. *J. Phys. Chem. C* **2010**, *114*, 4228–4236. (e) De Marco, L.; Manca, M.; Buonsanti, R.; Giannuzzi, R.; Malara, F.; Pareo, P.; Martiradonna, L.; Giancaspro, N. M.; Cozzoli, P. D.; Gigli, G. *J. Mater. Chem.* **2011**, *21*, 13371–13379. (f) Melcarne, G.; De Marco, L.; Carlino, E.; Martina, F.; Manca, M.; Cingolani, R.; Gigli, G.; Ciccarella, G. *J. Mater. Chem.* **2010**, *20*, 7248–7254. (g) Das, J.; Freitas, F. S.; Evans, I. R.; Nogueira, A. F.; Khushalani, D. *J. Mater. Chem.* **2010**, *20*, 4425–4431.

(31) (a) Wu, G. S.; Wang, J. P.; Thomas, D. F.; Chen, A. C. *Langmuir* **2008**, *24*, 3503–3509. (b) Abazovic, N. D.; Comor, M. I.; Zec, S.; Nedeljkovic, J. M.; Piscopiello, E.; Montone, A.; Antisari, M. V. *J. Am. Ceram. Soc.* **2009**, *92*, 894–896. (c) Sinha, A. K.; Jana, S.; Pande, S.; Sarkar, S.; Pradhan, M.; Basu, M.; Saha, S.; Pal, A.; Pal, T. *Cryst. Eng. Comm.* **2009**, *11*, 1210–1212. (d) Zhao, B.; Chen, F.; Huang, Q.; Zhang, J. *Chem. Commun.* **2009**, 5115–5117. (e) Ban, T.; Nakatani, T.; Uehara, Y.; Ohya, Y. *Cryst. Growth Des.* **2008**, *8*, 935–940. (f) Liu, M.; Piao, L.; Lu, W.; Ju, S.; Zhao, L.; Zhou, C.; Li, H.; Wang, W. *Nanoscale* **2010**, *2*, 1115–111. (g) Zhu, J.; Wang, S. H.; Bian, Z. F.; Cai, C. L.; Li, H. X. *Res. Chem. Intermed.* **2009**, *35*, 769–777.

(32) Li, Y.; Fan, Y.; Chen, Y. *J. Mater. Chem* **2002**, *12*, 1387–1390.

(33) Zhang, D.; Qi, L.; Ma, J.; Cheng, H. *J. Mater. Chem* **2002**, *12*, 3677–3680.

(34) Lai, T. M.; Yi, L.; Yang, W. X. *Chem. Lett.* **2010**, *39*, 294–295.

(35) Jun, Y.-w.; Casula, M. F.; Sim, J. H.; Kim, S. Y.; Cheon, J.; Alivisatos, A. P. *J. Am. Chem. Soc.* **2003**, *125*, 15981–15985.

(36) Joo, J.; Kwon, S. G.; Yu, T.; Cho, M.; Lee, J.; Yoon, J.; Hyeon, T. *J. Phys. Chem. B* **2005**, *109*, 15297–15302.

(37) Cottam, B. F.; Krishnadasan, S.; deMello, A. J.; deMello, J. C.; Shaffer, M. S. P. *Lab Chip* **2007**, *7*, 167–169.

(38) (a) Zhou, W. J.; Liu, H.; Boughton, R. I.; Du, G. J.; Lin, J. J.; Wang, J. Y.; Liu, D. *J. Mater. Chem.* **2010**, *20*, 5993–6008. (b) Sauvage, F.; Di Fonzo, F.; Li Bassi, A.; Casari, C. S.; Russo, V.; Divitini, G.; Ducati, C.; Bottani, C. E.; Comte, P.; Graetzel, M. *Nano Lett.* **2010**, *10*, 2562–2567. (c) Wang, H.; Bai, Y.; Wu, Q.; Zhou, W.; Zhang, H.; Li, J.; Guo, L. *Phys. Chem. Chem. Phys.* **2011**, *13*, 7008–7013. (d) Liao, W.-P.; Wu, J.-J. *J. Mater. Chem.* **2011**, *21*, 9255–9262.

(39) (a) Ito, S.; Chen, P.; Comte, P.; Nazeeruddin, M. K.; Liska, P.; Péchy, P; Grätzel, M. *Prog. Photovolt. Res. Appl.* **2007**, *15*, 603–612. (b) Ito, S.; Murakami, T. N.; Comte, P.; Liska, P.; Grätzel, C.; Nazeeruddin, M. K.; Grätzel, M. *Thin Solid Films* **2008**, *516*, 4613–4619.

(40) (a) Refinement of powder (Rietveld) and single-crystal diffraction data: http://www-llb.cea.fr/fullweb. (b) Järvinen, M. *J. Appl. Crystallogr.* **1993**, *26*, 525–531.

(41) Stadelmann, P. A. *Ultramicroscopy* **1987**, *21*, 131–145.

(42) (a) Weirich, T. E.; Winterer, M.; Seifried, S.; Hahn, H.; Fuess, H. *Ultramicroscopy* **2000**, *81*, 263–270. (b) Tonejc, A. M.; Djerdj, I.; Tonejc, A. *Mater. Sci. Eng., C* **2002**, *19*, 85–89. (c) Djerdj, I.; Tonejc, A. M. *J. Alloys Compd.* **2006**, *413*, 159–174. (d) Varghese, S.; David, M.; Barry, C. M.; Alexei, K.; Leonid, S. D.; Qing, D.; Vladimir, D. *Appl. Phys. Lett.* **2006**, *88*, 243103.

(43) Cozzoli, P. D.; Kornowski, A.; Weller, H. *J. Am. Chem. Soc.* **2003**, *125*, 14539–14548.

(44) Zhang, Z. H.; Zhong, X. H.; Liu, S. H.; Li, D. F.; Han, M. Y. *Angew. Chem., Int. Ed.* **2005**, *44*, 3466–3470.

(45) De Caro, L.; Carlino, E.; Caputo, G.; Cozzoli, P. D.; Giannini, C. *Nat. Nano.* **2010**, *5*, 360–365.

(46) (a) Valeeva, A. A.; Rempel, A. A.; Gusev, A. I. *Inorg. Mater.* **2001**, *37*, 603–612. (b) Chen, G. S.; Lee, C. C.; Niu, H.; Huang, W.; Jann, R.; Schutte, T. *Thin Solid Films* **2008**, *516*, 8473–8478. (c) Zárate, R. A.; Fuenzalida, V. M. *Vacuum* **2004**, *76*, 13–17. (d) Li, Z. G.; Miyake, S.; Makino, M.; Wu, Y. X. *Appl. Surf. Sci.* **2008**, *255*, 2370–2374. (e) Veljkovic, I.; Poleti, D.; Zdujic, M.; Karanovic, L.; Jovalekic, C. *Mater. Lett.* **2008**, *62*, 2769–2771. (f) Semaltianos, N. G.; Logothetidis, S.; Frangis, N.; Tsiaoussis, I.; Perrie, W.; Dearden, G.; Watkins, K. G. *Chem. Phys. Lett.* **2010**, *496*, 113–116. (g) Simon, P.; Pignon, B.; Miao, B.; Coste-Leconte, S.; Leconte, Y.; Marguet, S.; Jegou, P.; Bouchet-Fabre, B.; Reynaud, C.; Herlin-Boime *Chem. Mater.* **2010**, *22*, 3704–3711.

(47) Buonsanti, R.; Grillo, V.; Carlino, E.; Giannini, C.; Kipp, T.; Cingolani, R.; Cozzoli, P. D. *J. Am. Chem. Soc.* **2008**, *130*, 11223–11233.

(48) Kwon, S. G.; Hyeon, T. *Acc. Chem. Res.* **2008**, *41*, 1696–1709.

(49) (a) Peng, Z. A.; Peng, X. G. *J. Am. Chem. Soc.* **2001**, *123*, 1389–1395. (b) Peng, X. *Adv. Mater.* **2003**, *15*, 459–463.

(50) Granasy, L.; Pusztai, T.; Tegze, G.; Warren, J. A.; Douglas, J. F. *Phys. Rev. E* **2005**, *72*, 011605.

(51) Penn, R. L.; Banfield, J. F. *Am. Mineral.* **1999**, *84*, 871–876.

(52) Ganduglia-Pirovano, M. V.; Hofmann, A.; Sauer, J. *Surf. Sci. Rep.* **2007**, *62*, 219–270.

(53) Mullin, J. W. *Crystallization*, 4th ed; Butterworth-Heinemann: Oxford, 2001.

(54) Cozzoli, P. D.; Manna, L.; Curri, M. L.; Kudera, S.; Giannini, C.; Striccoli, M.; Agostiano, A. *Chem. Mater.* **2005**, *17*, 1296–1306.

(55) Kim, Y. H.; Jun, Y. W.; Jun, B. H.; Lee, S. M.; Cheon, J. W. *J. Am. Chem. Soc.* **2002**, *124*, 13656–13657.

(56) Pietsch, U.; Holý, V.; Baumbach, T. *High-resolution X-ray scattering from thin films to lateral nanostructures*, 2nd ed.; Springer: New York, 2004.

(57) (a) Nazeeruddin, M. K.; Humphry-Baker, R.; Liska, P.; Grätzel, M. *J. Phys. Chem. B* **2003**, *107*, 8981–8987. (b) Grätzel, M. *Pure Appl. Chem.* **2001**, *73*, 459–467. (c) Adachi, M.; Murata, Y.; Takao, J.; Jiu, J.; Sakamoto, M.; Wang, F. *J. Am. Chem. Soc.* **2004**, *126*, 14943–14949. (d) De Angelis, F.; Fantacci, S.; Selloni, A.; Nazeeruddin, M. K.; Grätzel, M. *J. Phys. Chem. C* **2010**, *114*, 6054–6061.

(58) Chen, Y.; Kang, K. S.; Yoo, K. H.; Jyoti, N.; Kim, J. *J. Phys. Chem. C* **2009**, *113*, 19753–19755.

(59) Grätzel, M. *J. Photochem. Photobiol. C* **2003**, *4*, 145–153.

(60) (a) Gómez, M.; Magnusson, E.; Olsson, E.; Hagfeldt, A.; Lindquist, S. E.; Granqvist, C. G. *Sol. Energy Mater. Sol. Cells* **2000**, *62*, 259–263. (b) Park, N. G.; Van de Lagemaat, J.; Frank, A. J. *J. Phys. Chem. B* **2000**, *104*, 8989–8994. (c) Chappel, S.; Zaban, A. *Sol. Energy Mater. Sol. Cells* **2002**, *71*, 141–152.

(61) Hoshikawa, T.; Yamada, M.; Kikuchi, R.; Eguchi, K. *J. Electrochem. Soc.* **2005**, *152*, E68–E73.

(62) Wang, Q.; Moser, J. E.; Grätzel, M. *J. Phys. Chem. B* **2005**, *109*, 14945–14953.

(63) Hoshikawa, T.; Kikuchi, R.; Eguchi, K. *J. Electroanal. Chem.* **2006**, *558*, 59–67.

(64) Adachi, M.; Sakamoto, M.; Jiu, J.; Ogata, Y.; Isoda, S. *J. Phys. Chem. B* **2006**, *110*, 13872–13880.

(65) Halme, J.; Vahermaa, P.; Miettunen, K.; Lund, P. *Adv. Mater.* **2010**, *22*, E210–E234.

(66) Fabregat-Santiago, F.; Garcia-Belmonte, G.; Mora-Sero, I.; Bisquert, J. *Phys. Chem. Chem. Phys.* **2011**, *13*, 9083–9118.

(67) Wang, M.; Chen, P.; Humphry-Baker, R.; Zakeeruddin, S. M.; Grätzel, M. *Chem. Phys. Chem.* **2009**, *10*, 290–299.

(68) Bisquert, J.; Fabregat-Santiago, F.; Mora-Serò, I.; Garcia-Belmonte, G.; Gimènez, S. *J. Phys. Chem. C* **2009**, *113*, 17278–17290.

(69) Usami, A.; Ozaki, H. *J. Phys. Chem. B* **2001**, *105*, 4577–4583.

(70) Bisquert, J.; Zaban, A.; Salvador, P. *J. Phys. Chem. B* **2002**, *106*, 8774–8782.